The forbidden high-ionization-line region of the type 2 quasar SDSS J11311.05+162739.5: a clear view of the inner face of the torus?

M. Rose,[1]⋆ C. N. Tadhunter,[1]⋆ J. Holt,[2] C. Ramos Almeida[1] and S. P. Littlefair[1]

[1]*Department of Physics and Astronomy, University of Sheffield, Sheffield S3 7RH*
[2]*Leiden Observatory, Leiden University, PO Box 9513, 2300 RA Leiden, the Netherlands*

ABSTRACT

We present spectroscopic observations of the type 2 quasar SDSS J11311.05+162739.5 ($z = 0.1732$), which has the richest spectrum of forbidden high-ionization lines (FHILs, e.g. [Fe VII], [Fe X], [Fe XI] and [Ne V]) yet reported for an active galactic nucleus (AGN), as well as unusually strong [O III] $\lambda 4363$ emission. The study of this object provides a rare opportunity to investigate the physical conditions and kinematics of the region(s) emitting the FHILs. By comparison with photoionization model results, we find that the FHIL region has high densities ($10^{5.5} < n_H < 10^{8.0}\,\mathrm{cm}^{-3}$) and ionization parameters ($-1.5 < \log[U] < 0$), yet its kinematics are similar to those of the low-ionization emission-line region detected in the same object (full width at half-maximum $\sim 360 \pm 30\,\mathrm{km\,s}^{-1}$), with no evidence for a significant shift between the velocity centroid of the FHILs and the rest frame of the host galaxy. The deduced physical conditions lie between those of the broad-line ($n_H > 10^9\,\mathrm{cm}^{-3}$) and narrow-line regions ($n_H < 10^6\,\mathrm{cm}^{-3}$) of AGNs, and we demonstrate that the FHIL regions must be situated relatively close to the illuminating AGN ($0.32 < r_{FHIL} < 50\,\mathrm{pc}$). We suggest that the inner torus wall is the most likely location for the FHIL region, and that the unusual strength of the FHILs in this object is due to a specific viewing angle of the far wall of the torus, coupled with a lack of dust on larger scales that might otherwise obscure our view of the torus.

Key words: galaxies: active – galaxies: individual: SDSS J113111.05+162739.5 – quasars: emission lines – galaxies: Seyfert.

1 INTRODUCTION

Most Seyfert galaxies show some spectral lines from forbidden transitions of highly ionized ions in their spectra, for example, [Fe VII], [Fe X], [Fe XI] and even [Fe XIV] (Penston et al. 1984). These emission lines are often blueshifted with respect to the rest frame of the active galactic nucleus (AGN), and have velocity widths which are between those of the narrow-line region (NLR) and the broad-line region (BLR, Penston et al. 1984; Appenzeller & Wagner 1991; Mullaney et al. 2009). In some rare cases, many forbidden high-ionization lines (FHILs) of relatively high equivalent width (EW) have been detected. Examples include III Zw 77 (Osterbrock 1981), Tololo 0109-383 (Fosbury & Sansom 1983) and ESO 138 G1 (Alloin et al. 1992).

The physical mechanisms and conditions that allow strong FHILs to be produced have been debated for some time: whether there is a continuity from the photoionization processes which produce the lower ionization lines in the NLR (Korista & Ferland 1989; Ferguson 1997), or there is an entirely different mechanism for their formation (e.g. collisional excitation in a high-temperature gas; Nussbaumer & Osterbrock 1970).

Given that the transitions associated with many of the FHILs have high critical densities ($n_c > 10^5\,\mathrm{cm}^{-3}$), it has been suggested that they may originate in the innermost torus wall facing the illuminating source. Studies of the high critical density [Fe VII] $\lambda 6086$ emission line across Seyfert galaxies from types 1 and 2, including intermediate types, find that its strength increases relative to the low-ionization lines from type 2 to type 1. This can be interpreted in terms of the orientation-based division between Seyfert types (e.g. Antonucci 1993): as the Seyfert type gets closer to a Seyfert 1, more of the emission from the inner torus becomes visible to the observer (see Murayama & Taniguchi 1998; Nagao, Murayama & Taniguchi 2001). Therefore, the high critical density lines that are preferentially emitted by the torus are likely to be stronger in type 1 objects, as observed. However, to date the idea that the [Fe VII] emission lines are associated with the torus has not been thoroughly tested using detailed emission-line ratios that measure physical conditions accurately.

Although it seems plausible that at least some of the FHIL emission arises in the torus, the causes of the diversity in both the relative strength and the kinematics of the FHILs remain uncertain.

⋆E-mail: m.rose@sheffield.ac.uk (MR); c.tadhunter@sheffield.ac.uk (CNT)

One possibility is that the unusually strong FHILs observed in some objects are symptomatic of a recent energetic occurrence which is able to illuminate the region that produces these lines (Komossa et al. 2009); suggestions for such events include the rapid accretion of material from the interstellar medium, the tidal disruption of a star by the supermassive black hole (SMBH), gamma-ray bursts and supernovae (Komossa et al. 2009).

The unusual strength of the FHILs in objects such as III Zw 77, Tololo 0109-383 and ESO 138 G1 provides us with a rare opportunity to study the nature of the region of the AGN which emits them, and thus helps us to better understand the structure of AGNs in general.

This paper reports an investigation of the object SDSS J11311.05+162739.5 (hereafter Q1131+16), which has the richest spectrum of FHILs yet reported for an AGN. Q1131+16 was discovered in the 2MASS survey and was classified as a Seyfert 2 galaxy with a redshift of 0.174. It belongs to a sample of quasar-like objects identified on the basis of their red near-infrared (near-IR) colours [$(J - K) > 2.0$)] in the 2MASS (Cutri 1995). In this paper, we present deep optical and IR spectra of Q1131+16 and use these to deduce the physical conditions and kinematics of the FHIL emission lines, with the aim of investigating their origin. The cosmological parameters used throughout this paper are adopted from the *WMAP*: $H_0 = 71 \, \text{km s}^{-1}$, $\Omega_M = 0.27$ and $\Omega_\Lambda = 0.73$ (Spergel et al. 2003), resulting in a spatial scale of 3.46 kpc arcsec^{-1}.

2 OBSERVATIONS AND DATA REDUCTION

2.1 ING ISIS observations

Low-resolution optical spectroscopic observations of Q1131+16 were taken on 2007 February 9 with the ISIS dual-arm spectrograph on the 4.2-m William Herschel Telescope (WHT) on La Palma as part of a spectroscopic survey of a representative sample of red, quasar-like objects. The full sample for this survey comprised of a complete right ascension limited subsample of 24 objects with near-IR colours $(J - K) > 2$ and $z < 0.2$ selected from the list of Hutchings et al. (2003), which is itself representative of the population of red, 2MASS-selected quasars. The unusually strong FHILs in Q1131+16 were discovered serendipitously in the course of this survey.

In the red the *R158R* grating was used with the REDPLUS CCD, while in the blue the *R300B* grating was used with the EEV12 CCD. A dichroic at 5300 Å was employed to obtain spectra with the useful wavelength ranges ~3250–5250 Å in the blue and ~5200–9500 Å in the red. To reduce the effects of differential refraction, all exposures were taken when Q1131+16 was at low airmass (sec $z < 1.1$), and with the slit aligned close to the parallactic angle. The seeing for the night of the observations varied from 0.8 to 1.3 arcsec (full width at half-maximum, hereinafter FWHM).[1]

Sets of three 600-s exposures were taken on both arms simultaneously, giving a total exposure time of 1800 s. The data were taken with a 1.5-arcsec slit along a position angle (PA) 315°. To eliminate the contamination from the second-order emission, a GG495 blocking filter was introduced into the ISIS red arm.

The data were reduced in the standard way (bias subtraction, flat-fielding, cosmic-ray removal, wavelength calibration, flux cali-

bration) using packages in IRAF.[2] The 2D spectra were also corrected for spatial distortions of the CCD. To reduce wavelength calibration errors due to the flexure of the telescope and instrument, arc spectra were taken at the position of the object on the sky; the estimated wavelength calibration accuracy is 0.1 Å in both the blue and the red (however, this may be an underestimate at the extreme edges of the spectra). The atmospheric absorption features were removed by dividing by the spectrum of a telluric standard (BD+17 2352), taken close in time and airmass to the observations of Q1131+16. The spectral resolution, calculated using the widths of the night sky emission lines, was 6.11 ± 0.74 Å in the blue and 10.96 ± 0.83 Å in the red (measured in the observed frame of the spectrum). The spatial pixel scales of the 2D spectra are 0.4 arcsec in the blue and 0.44 arcsec in the red, and the relative flux calibration uncertainty – based on 11 observations of eight flux standard stars taken throughout the run – is estimated to be ±5 per cent.

The spectra were extracted and analysed using the Starlink packages FIGARO and DIPSO.

2.2 Gemini GMOS observations

In order to test the possibility that the emission lines of Q1131+16 are variable, a follow-up spectrum was taken using the GMOS on the Gemini south telescope at Cerro Pachon.

Spectroscopic and imaging observations using the GMOS were taken on 2010 February 21 during the Gemini queue observation time as part of the programme GS-2009B-Q-87. The spectral observations comprised three 600-s exposures using a central wavelength 5000 Å at an airmass of 1.46, and a 1.5-arcsec slit aligned along PA $= 163°$ – close to the parallactic angle for the centre of the observations. This resulted in a spectrum with a useful wavelength range ~3700–6450 Å. The observations of the flux standard star, Feige56, had the same set-up but with an exposure time of 10 s, taken at an airmass of 1.61 and with a 5-arcsec slit. Deep GMOS images were also taken using an *r′* filter at an airmass of 1.56. Each exposure of the imaging observations had an exposure time of 250 s, and the data were taken in a four-point dither pattern, resulting in a total exposure time of 1000 s. The seeing was estimated to be 0.75 ± 0.02 arcsec (FWHM), based on measurements of stars in the GMOS image.

The spectra were extracted and analysed using the Starlink packages FIGARO and DIPSO, and the IRAF packages GEMINI and NOAO. An analysis of the night sky lines implies a wavelength calibration uncertainty of 0.50 ± 0.06 Å for the spectrum. The spectral resolution, calculated using the widths of the night sky emission lines, was 7.12 ± 0.11 Å in the observed frame of the observations, and the spatial pixel scale is 0.147 arcsec pixel^{-1}.

Comparisons between the WHT and Gemini spectra demonstrate that the fluxes of the stronger emission lines (e.g. [O III] $\lambda\lambda4363,4959,5007$, [Ne V] $\lambda3426$, [Fe VII] $\lambda 3759$) and continuum agree within 20 per cent between the two sets of observations. This is remarkable considering that the two sets of observations were taken with different instruments, at different slit PAs and under different seeing conditions.

The GMOS image was reduced using the standard Gemini pipeline reduction software. The photometric calibration used the

---

[1] Unfortunately, due to a lack of suitable imaging observations, an accurate seeing estimate does not exist for the exact time of the WHT observations of Q1131+16.

[2] IRAF is distributed by the National Optical Astronomy Observatory, which is operated by the Association of Universities for the Research in Astronomy, Inc., under cooperative agreement with the National Science Foundation (http://iraf.noao.edu/).

zero-point magnitude for the r' filter advertised on the GMOS south website, taking the full account of the airmass and exposure time of the observations.

2.3 ING LIRIS observations

On the night starting on 2010 March 2, we obtained a 1.388–2.419 μm spectrum of Q1131+16 using the HK grism in the LIRIS (Manchado et al. 1998) on the 4.2-m WHT on La Palma. The spectrum has a dispersion of 9.7 Å pixel^{-1}, and a 1-arcsec slit was used, giving a spectral resolution of ∼40 Å. The seeing was approximately 2 arcsec and the night suffered from heavy cirrus. A total exposure time of 88 min was obtained over airmasses ranging from 1.0 to 2.2. The total exposure was divided into 240-s subexposures and the telescope was nodded in the standard manner to aid sky subtraction. A random jitter of 10 arcsec was added to the default nod positions to limit the impact of bad pixels. Observations of the A5V star BD+16 2325 were also taken to correct for the effects of telluric absorption and to provide a relative flux calibration. Both stars were observed with a slit PA of 0°. For a more detailed description of the reduction process, see Ramos Almeida, Pérez García & Acosta-Pulido (2009).

3 RESULTS

3.1 Spatial distribution of the emission lines

While our 2D spectra show that all the emission lines are strongly concentrated in the nucleus of the host galaxy, we detect spatially extended line emission in [O II] λ3727 (see Fig. 1), Hβ, [O III] λλ5007,4959 and the Hα+[N II] blend. The emission lines have a maximum extent of 9 arcsec in the north–south direction (29 kpc) in the Gemini spectrum (PA = 163°) and 15 arcsec in the north-west–south-east direction (47 kpc) in the WHT spectra (PA = 315°), corresponding to the spatial extent of the galaxy disc visible in our Gemini r' image (see Section 3.5).

In order to investigate the nuclear spectrum, we extracted apertures of size 1.5×1.5 arcsec^2 from the 2D WHT and Gemini spectra. The apertures were centred on the nucleus.

To determine the spatial distributions of both the emission lines and the continuum along the slit, spatial slices were extracted from the 2D WHT spectrum over the wavelength ranges given in Table 1. The continuum slices were extracted with similar wavelength ranges to their nearby emission lines so that the continuum could be accurately subtracted from the slices containing the emission lines. The DIPSO Starlink package was then used to measure the centroid and spatial FWHM of the flux distribution of each slice, by fitting a single-Gaussian profile to the central cores of the emission.

Overall, the centroids measured for each emission line and continuum slice in Table 1 are all consistent within their uncertainties, implying no spatial offset between any of the emission lines individually, nor between the emission lines and the continuum.

The spatial FWHMs of all the emission lines – with the exception of [O II] λ3727 – are consistent with the seeing on the night of the observations (see Section 2.1), suggesting that their spatial distributions are unresolved in the observations. Therefore, the spatial distributions of the high-ionization lines provide an indication of the true seeing of the WHT observations (1.1 < FWHM < 1.35 arcsec). As expected, there is evidence that the seeing degrades towards shorter wavelengths, since the two shortest wavelength FHILs have significantly larger spatial FWHMs than their longer wavelength counterparts. Moreover, the fact that the spatial FWHM measured for all continuum slices significantly exceeds the estimated seeing demonstrates that the continuum emission is spatially resolved in the nuclear regions.

The spatial FWHM of the [O II] λ3727 emission line is significantly broader than the other FHILs at similar wavelengths in Table 1 and this line is clearly resolved in the 2D spectrum (see Fig. 1). The combination of the large spatial extent and spatially resolved nuclear emission of [O II] makes this emission line ideal for the study of the emission-line kinematics across the host galaxy Q1131+16 presented in Section 3.6.

3.2 Line identifications

The optical spectra of Q1131+16 are shown in Figs 2–5. What makes the spectrum of Q1131+16 special is not only the large
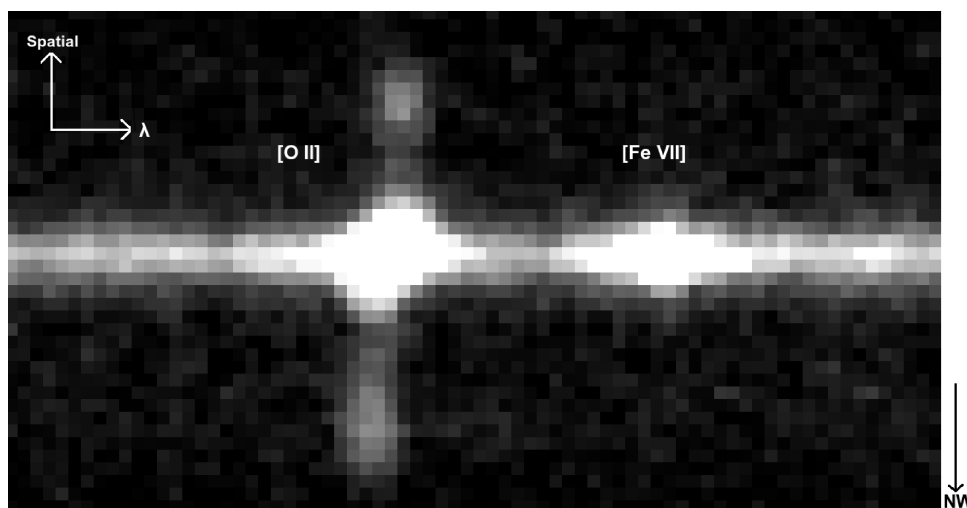

Figure 1. A section of the 2D WHT spectrum along PA = 315° showing [O II] λ3727 and [Fe VII] λ3759. Note that [O II] is extended 6.9 arcsec above and 8.1 arcsec below the continuum of Q1131+16 and is well resolved. The spatial direction of the slit is indicated along side the plot. In addition, a nuclear velocity gradient in [O II] can be seen from the fact that its profile is slanted when compared to that of [Fe VII].

Table 1. Centroid positions and spatial extents of selected emission lines and the continuum at different wavelength intervals, as measured from the 2D WHT spectrum. The centroids (measured in pixels) and the FWHM (measured in arcseconds) were determined using single-Gaussian fits to the bright cores of the spatial distributions of the emission lines along the slit.

λ_{Rest} (Å)	Range (Å)	Centroid	±	FWHM (arcsec)	±
Blue arm					
[Ne v] 3425	35	98.34	0.01	1.35	0.01
Continuum 3392	35	98.23	0.04	1.71	0.04
[O ii] 3727	45	98.39	0.08	1.56	0.06
Continuum 3690	45	98.21	0.07	1.78	0.06
[Fe vii] 3759	45	98.32	0.07	1.28	0.05
[Ne iii] 3868	45	98.32	0.01	1.24	0.01
Continuum 3923	45	98.33	0.06	1.81	0.07
Hδ	50	98.49	0.05	1.04	0.05
Continuum 4147	50	98.25	0.06	1.74	0.06
Hγ	35	98.33	0.04	1.09	0.04
[O iii] 4363	35	98.35	0.05	1.14	0.02
Continuum 4466	35	98.38	0.05	1.73	0.07
Red arm					
He ii 4686	50	89.82	0.12	1.25	0.15
Continuum 5545	50	89.84	0.04	1.74	0.05
Hβ	50	89.74	0.04	1.09	0.04
[O iii] 4959,5007	130	89.75	0.01	1.18	0.01
Continuum 5093	130	89.85	0.04	1.74	0.05
[Fe vii] 6086	65	89.83	0.02	1.19	0.02
Continuum 6139	65	89.80	0.04	1.87	0.05
Hα	145	89.81	0.01	1.09	0.02
Continuum 6435	145	89.81	0.04	1.71	0.05
[Fe xi] 7892	40	89.76	0.10	1.18	0.11
Continuum 7927	40	89.84	0.06	1.80	0.07

number of emission lines, but also their rich variety. In particular, the detected FHILs include [Fe v] λλ3839,3891,4181, [Fe vi] λλ5146,5176,5335, [Fe vii] λλ3759,4893,5159,5276,5720,6086, [Fe x] λ6375, [Fe xi] λ7891 and [Ne v] λλ3346,3426.[3] As well as the FHILs, lower ionization species which are not typically detected in quasar spectra are found in the spectrum, including [Fe iv] λλ2829,2836,4903,5236, along with Bowen resonance fluorescence lines of O iii, such as O iii λ3133. Also detected are more typical AGN emission lines such as Hα, Hβ, He ii λ4686, [O ii] λλ3726,3729 and [O iii] λλ4363,4959,5007. However, the FHILs are unusually strong with respect to the latter lines, with [Ne v] λ3426 comfortably exceeding the strength of the [O ii] λ3727 doublet and [Fe vii] λ6086 of comparable strength to Hβ. Also notable is the unusual strength of [O iii] λ4363 compared to Hγ and [O iii] λ5007 ([O iii] (λ5007/4363) = 5.86 ± 0.21 in the WHT spectrum), as well as the relatively modest ratio of [O iii] λ5007 to Hβ ([O iii]/Hβ=5.27 ± 0.16), given the strength of the other high-ionization lines.

The strongest emission lines in this object have relatively large EWs, including a large number of FHILs with EWs comparable to other typical lower ionization emission lines. Indeed, the EWs of the FHILs in Q1131+16 are larger than those of any other AGN with published spectra, including other objects with unusually strong FHILs such as III Zw 77 (Osterbrock 1981) and

Tololo 0109-383 (Fosbury & Sansom 1983). Moreover, the [O iii] emission-line luminosity of Q1131+16 [(4.6 ± 0.1) × 10⁸ L⊙] would lead to its classification as a type 2 quasar object according to the criterion of Zakamska et al. (2003). Overall, the rich variety of emission lines, and their relatively large EWs, allow for a thorough investigation of the physical conditions of the FHIL emission region.

A full list of line identifications made from these spectra is presented in Table 2. All the line identifications have been determined by fitting single Gaussians to the emission features in both the WHT and Gemini spectra. The rest-frame wavelength ranges that were fitted for Q1131+16 are 2700–4600 and 4600–8000 Å in the WHT spectra, and 3100–5450 Å in the Gemini spectrum. Table 2 gives the line flux ratios relative to Hβ for both spectra. The fluxes of the emission lines have not been corrected for intrinsic reddening for reasons that will become clear in Section 3.8. In addition, it appears that there is no need of a Galactic extinction correction, since the IRSA extinction tool in the NASA/IPAC Extragalactic Database (NED) gives a reddening of only $E(B - V) = 0.031$ (Schlegel, Finkbeiner & Davis 1998).

The majority of line identifications have been confirmed in other astrophysical objects such as AGNs and planetary nebulae (e.g. Kaler 1976; Osterbrock 1981; Fosbury & Sansom 1983; Alloin et al. 1992). However, there are several emission lines in Table 2 which have been identified using the National Institute of Standards and Technology (NIST) spectral line data base (see reference 4 in Table 2). An emission line was only regarded as a secure ID if its line centre was within 1.5σ of the wavelength predicted for

---

[3] In this study, we define a FHIL as an emission species with an ionization potential greater than or equal to 54.4 eV (that of He ii).
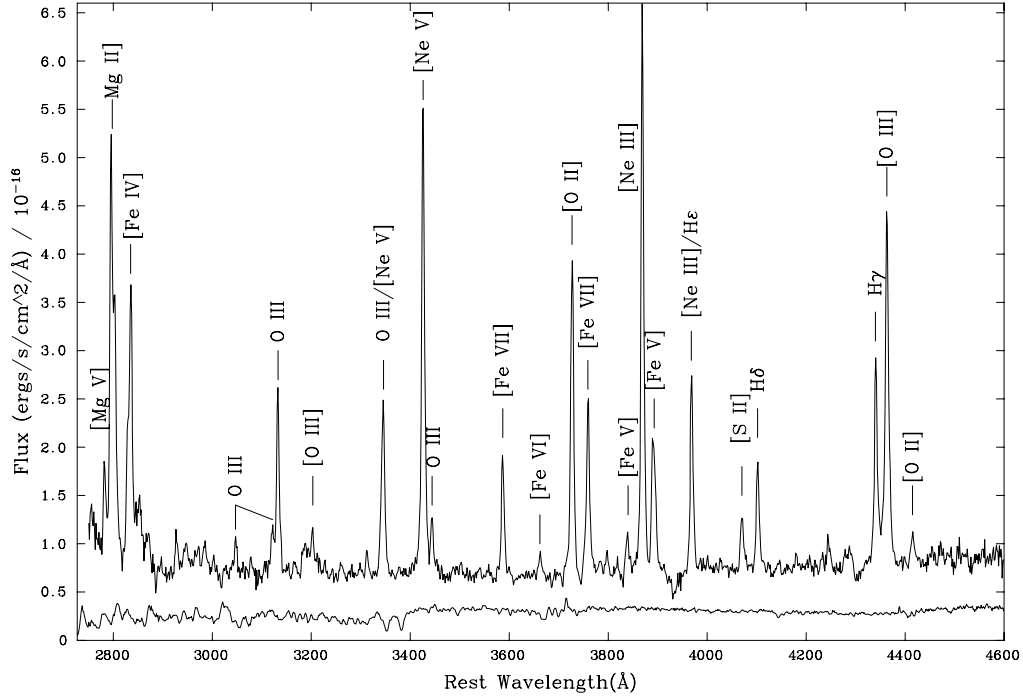
Figure 2. WHT nuclear spectrum of Q1131+16 taken on the ISIS blue arm. Unresolved blends are indicated by an '/', while resolved blends are indicated by an '&'. The flux scale is measured in units of 10^{-16} erg s^{-1} Å^{-1} cm^{-2}. Note the strength of high-ionization lines such as [Ne v] and [Fe vii] relative to [O ii], and of [O iii] λ4363 relative to Hδ. For reference, we also show a scaled version of the night sky spectrum extracted from the 2D frames at the bottom of the plot.
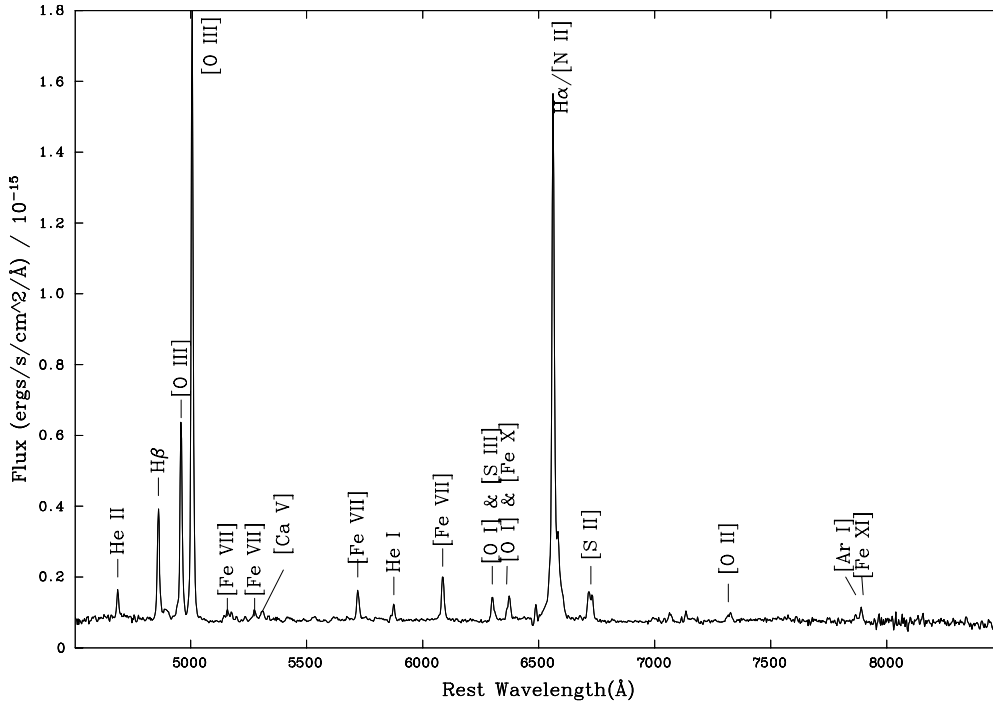

Figure 3. WHT nuclear spectrum of Q1131+16 taken on the ISIS red arm. The flux scale is measured in units of 10^{-15} erg s^{-1} Å^{-1} cm^{-2}.

that particular emission line based on the mean redshift, and if its signal-to-noise ratio exceeded 3.0. As well as the 66 identified emission lines, there are 37 emission lines which remain unidentified (see Table 3), in the sense that there are no IDs for them in the NIST spectral line data base that give redshifts within 1.5σ of the mean

redshift, yet their S/N exceeds 3. Note that, due to its higher S/N, the Gemini spectrum reveals a large number of faint lines that were not detected in the original WHT spectrum (see Tables 2 and 3).

Interestingly, although there are many iron FHILs in the spectrum of Q1131+16, there is no clear evidence for the [Fe xiv] λ5303
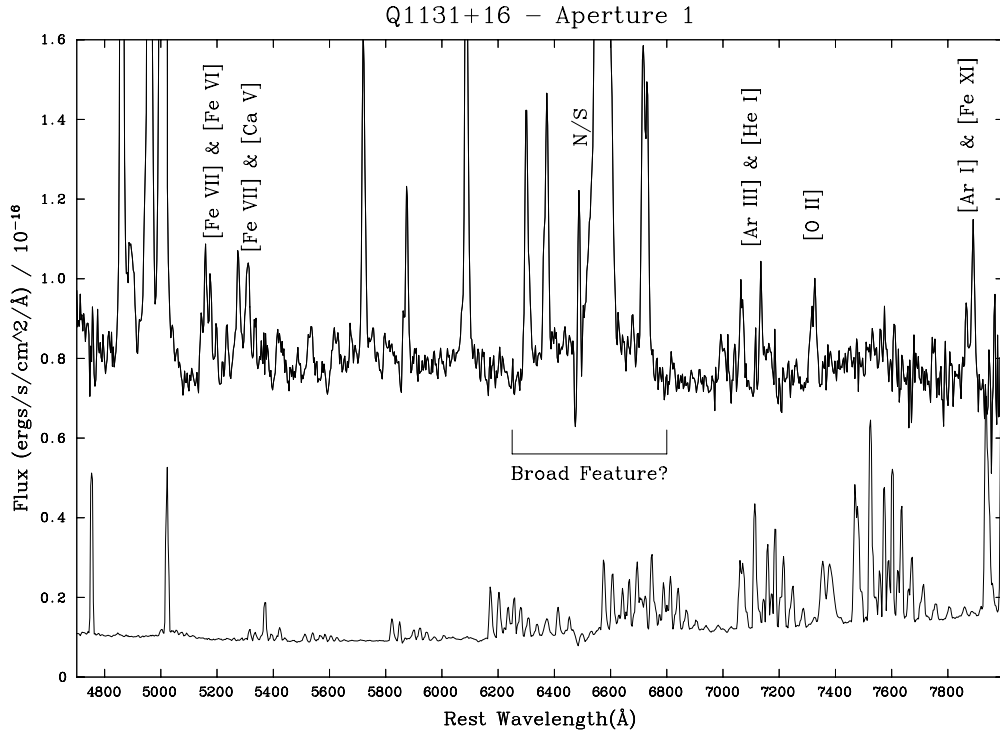
Figure 4. An expanded plot of the Q1131+16 ISIS red arm spectrum. This has been presented to highlight the weaker features in the red spectrum. The flux scale is measured in units of 10^{-16} erg s^{-1} Å^{-1} cm^{-2}. As well as the multitude of high-ionization lines, note the broad base to the Hα +[N II] blend. For reference, we also show a scaled version of the night sky spectrum extracted from the 2D frames at the bottom of the plot.
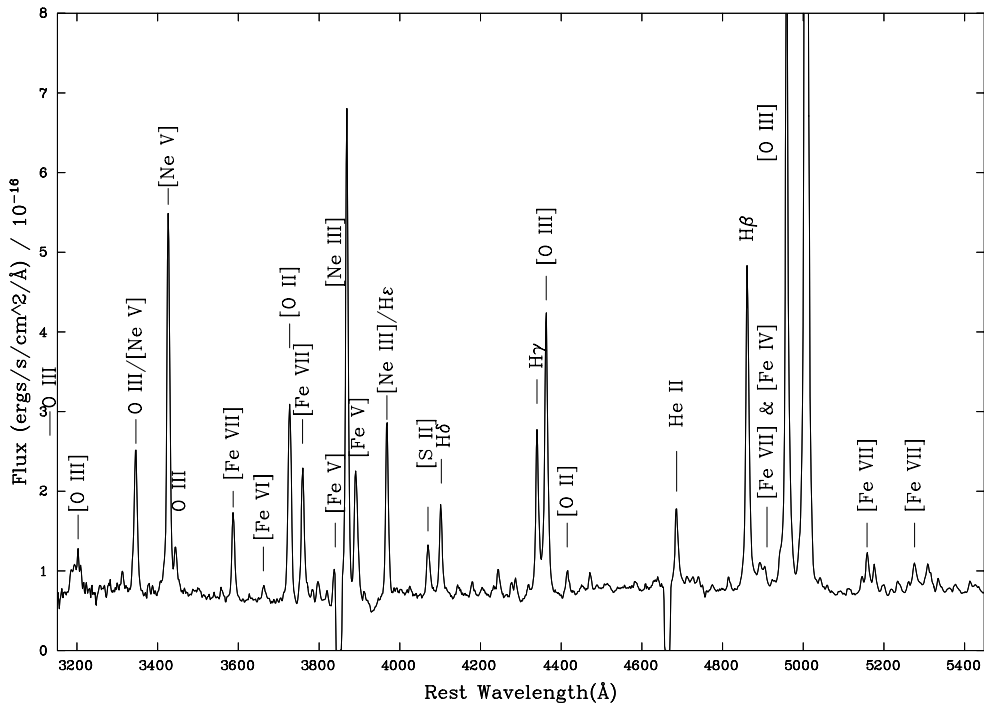

Figure 5. Nuclear spectrum of Q1131+16 taken using the GMOS on the Gemini South telescope. The flux scale has been narrowed here to highlight how rich the spectrum is in emission lines. The flux scale is measured in units of 10^{-16} erg s^{-1} Å^{-1} cm^{-2}. The gaps in the spectrum are due to the gaps between the CCD chips in the GMOS instrument.

emission line. The identification of this emission feature at ∼5300 Å has been controversial in the past: it has been debated whether it is [Fe XIV] λ5303 or [Ca V] λ5309 (e.g. Oke & Sargent 1968; Weedman 1971). When this feature is fitted in our WHT spectrum, if only the

[Ca V] λ5309 identification is considered, the individual redshift of the emission line (0.17319 ± 0.000 11 for the WHT spectrum) agrees within the uncertainties with the average redshift of all the lines (0.173 25 ± 0.000 01, see Section 3.6). However, if the feature

Table 2. Line identifications for the nuclear spectra of Q1131+16. Flux ratios are relative to Hβ and are not corrected for reddening. Line IDs and redshifts are determined by fitting a single Gaussian to the emission lines. Errors for the measured wavelengths and redshifts include calibration errors as well as errors due to the measurement techniques. The total flux of the Hβ emission line is $(4.38 \pm 0.11) \times 10^{-15}$ and $(4.74 \pm 0.11) \times 10^{-15}$ erg s^{-1} cm^{-3} for the WHT and Gemini spectra respectively. Reference key: (1) Osterbrock (1981); (2) Siegel et al. (1998); (3) Osterbrock & Ferland 2006; (4) identified using the NIST data base (Ralchenko et al. 2010); (5) Meinel et al. (1975); (6) Kaler (1976); and (7) Tran et al. (1998). Notes key: (1) the broad-line components were not modelled for these emission features to avoid negative flux results for their line fluxes; and (2) the narrow-line components were not modelled for these emission features to avoid negative flux results for their line fluxes. Notes (1) and (2) refer to the WHT and Gemini spectra, respectively.

Line ID	λ (Å)	λ$_{WHT}$ (Å)	(F/F$_{Hβ}$) (WHT)	Z$_{WHT}$	λ$_{Gemini}$ (Å)	(F/F$_{Hβ}$) (Gemini)	Z Gemini	Reference	Notes (1)	Notes (2)
Mg V	2782.7	3264.7 ± 0.36	0.158 ± 0.024	0.1732 ± 1.1E−04	—	—	—	7	—	—
Mg II	2795.5	3279.7 ± 0.60	0.630 ± 0.126	0.1732 ± 1.5E−04	—	—	—	2	—	—
Mg II	2802.7	3287.9 ± 0.71	0.549 ± 0.129	0.1731 ± 1.5E−04	—	—	—	2	—	—
[Fe IV]	2829.3	3319.6 ± 0.60	0.199 ± 0.021	0.1733 ± 1.3E−04	—	—	—	4	1	—
[Fe IV]	2835.7	3326.9 ± 0.52	0.419 ± 0.021	0.1732 ± 1.0E−04	—	—	—	4	1	—
O III	3132.9	3675.2 ± 0.52	0.358 ± 0.027	0.1731 ± 1.4E−04	3675.8 ± 0.51	0.382 ± 0.041	0.1733 ± 1.4E−04	1	—	—
He I	3187.7	3740.1 ± 0.61	0.081 ± 0.010	0.1733 ± 2.6E−04	3738.7 ± 0.70	0.074 ± 0.006	0.1729 ± 1.9E−04	4	2	2
He II	3202.7	3757.2 ± 0.97	0.095 ± 0.024	0.1731 ± 2.6E−04	3757.6 ± 0.55	0.079 ± 0.006	0.1733 ± 1.5E−04	6	—	—
[O III]	3312.3	3886.6 ± 0.64	0.037 ± 0.004	0.1734 ± 1.8E−04	3885.0 ± 2.10	0.034 ± 0.003	0.1729 ± 5.4E−04	4	1	1
[Ne V]	3425.9	4019.5 ± 0.50	1.010 ± 0.085	0.1733 ± 1.2E−04	4020.2 ± 0.52	1.051 ± 0.035	0.1735 ± 1.3E−04	1	—	—
[N I]	3466.0	—	—	—	4067.0 ± 1.80	0.026 ± 0.003	0.1734 ± 4.4E−04	6	—	1
He I	3487.6	—	—	—	4092.3 ± 1.70	0.023 ± 0.003	0.1734 ± 4.2E−04	6	—	—
[Fe VI]	3662.5	4297.2 ± 0.51	0.051 ± 0.011	0.1733 ± 1.4E−04	4298.0 ± 1.10	0.042 ± 0.006	0.1735 ± 2.6E−04	1	—	—
H I	3704.9	—	—	—	4346.7 ± 0.52	0.011 ± 0.002	0.1732 ± 1.2E−04	6	—	2
[O II]	3726.0	4371.9 ± 0.61	0.597 ± 0.028	0.1733 ± 1.1E−04	4371.6 ± 0.59	0.513 ± 0.039	0.1733 ± 1.3E−04	1	—	—
[O II]	3728.8	4375.1 ± 0.63	0.156 ± 0.049	0.1733 ± 1.1E−04	4374.7 ± 0.60	0.131 ± 0.025	0.1732 ± 1.1E−04	1	—	—
[Fe VII]	3758.9	4410.5 ± 0.51	0.421 ± 0.028	0.1733 ± 1.2E−04	4410.9 ± 0.51	0.395 ± 0.018	0.1735 ± 1.2E−04	1	—	—
H I	3797.9	—	—	—	4455.6 ± 0.80	0.036 ± 0.004	0.1732 ± 1.8E−04	6	—	2
He I	3819.3	—	—	—	4480.4 ± 0.80	0.023 ± 0.003	0.1731 ± 1.8E−04	6	—	2
[Fe V]	3839.3	4504.1 ± 0.91	0.084 ± 0.035	0.1731 ± 2.0E−04	4502.6 ± 0.52	0.069 ± 0.003	0.1728 ± 1.2E−04	1	—	—
[Ne III]	3868.8	4539.4 ± 0.50	1.103 ± 0.050	0.1733 ± 1.2E−04	4539.3 ± 0.79	1.359 ± 0.102	0.1733 ± 1.7E−04	1	—	—
[Fe V]	3891.3	4565.6 ± 0.56	0.363 ± 0.051	0.1733 ± 1.2E−04	4565.4 ± 0.60	0.533 ± 0.003	0.1732 ± 1.3E−04	1	—	—
[Ne III]	3967.5	4655.3 ± 0.51	0.449 ± 0.038	0.1733 ± 1.1E−04	4655.7 ± 0.59	0.466 ± 0.020	0.1735 ± 1.3E−04	1	—	—
He I	4026.2	—	—	—	4722.6 ± 1.10	0.013 ± 0.002	0.1730 ± 2.3E−04	6	—	2
[S II]	4068.6	4773.5 ± 0.50	0.098 ± 0.012	0.1733 ± 1.2E−04	4774.1 ± 0.58	0.142 ± 0.012	0.1734 ± 1.2E−04	1	—	—
[S II]	4076.3	4782.5 ± 0.50	0.021 ± 0.004	0.1733 ± 1.0E−04	4785.4 ± 0.58	0.019 ± 0.006	0.1740 ± 1.2E−04	3	2	—
Hδ	4101.7	4812.7 ± 0.51	0.240 ± 0.016	0.1733 ± 1.1E−04	4812.3 ± 0.50	0.240 ± 0.013	0.1732 ± 1.0E−04	1	—	—
[Fe V]	4180.2	—	—	—	4904.1 ± 0.52	0.040 ± 0.006	0.1730 ± 1.1E−04	6	—	—
[O II]	4317.2	—	—	—	5066.6 ± 0.50	0.056 ± 0.007	0.1736 ± 9.9E−05	6	—	—
Hγ	4340.5	5092.6 ± 0.50	0.438 ± 0.024	0.1733 ± 1.0E−04	5092.7 ± 0.61	0.454 ± 0.029	0.1733 ± 1.2E−04	1	—	—
[O III]	4363.2	5119.2 ± 0.50	0.899 ± 0.019	0.1733 ± 1.0E−04	5118.8 ± 0.59	0.839 ± 0.031	0.1732 ± 1.2E−04	1	—	—
[O II]	4414.9	5180.1 ± 0.78	0.067 ± 0.023	0.1733 ± 1.0E−04	5180.5 ± 0.55	0.075 ± 0.011	0.1734 ± 1.1E−04	4	—	—
He I	4471.4	—	—	—	5246.4 ± 0.50	0.044 ± 0.011	0.1733 ± 9.5E−05	6	—	—
He II	4685.7	5497.5 ± 0.63	0.207 ± 0.050	0.1733 ± 1.1E−04	5497.9 ± 0.51	0.234 ± 0.012	0.1733 ± 9.3E−05	1	—	—
[Ar IV]	4712.6	—	—	—	5528.6 ± 0.67	0.055 ± 0.010	0.1732 ± 1.2E−04	6	—	—

Table 2 – *continued*

Line ID	λ (Å)	$\lambda_{\rm WHT}$ (Å)	$(F/F_{\rm H\beta})$ (WHT)	$Z_{\rm WHT}$	$\lambda_{\rm Gemini}$ (Å)	$(F/F_{\rm H\beta})$ (Gemini)	Z Gemini	Reference	Notes (1)	Notes (2)
Hβ	4861.3	5703.5 ± 0.50	1.000 ± 0.000	0.1733 ± 1.0E−04	5703.8 ± 0.52	1.000 ± 0.000	0.1733 ± 9.1E−05	1	–	–
[Fe VII]	4893.4	5740.8 ± 0.51	0.055 ± 0.018	0.1732 ± 1.0E−04	5740.6 ± 0.52	0.057 ± 0.016	0.1731 ± 1.2E−04	4	–	–
[Fe IV]	4903.1	5753.0 ± 0.52	0.012 ± 0.004	0.1733 ± 1.2E−04	5753.1 ± 0.51	0.038 ± 0.011	0.1734 ± 1.2E−04	4	1	1
[O III]	4958.9	5817.7 ± 0.50	1.757 ± 0.085	0.1732 ± 1.0E−04	5818.1 ± 0.55	1.914 ± 0.053	0.1733 ± 9.5E−05	1	–	–
[O III]	5006.0	5874.0 ± 0.50	5.270 ± 0.155	0.1732 ± 1.0E−04	5874.3 ± 0.55	5.740 ± 0.158	0.1733 ± 9.4E−05	1	–	–
[Fe VI]	5145.8	6036.9 ± 0.52	0.053 ± 0.005	0.1732 ± 1.0E−04	6036.7 ± 0.65	0.047 ± 0.005	0.1731 ± 1.1E−04	1	–	–
[Fe VII]	5159.0	6052.7 ± 0.81	0.103 ± 0.030	0.1732 ± 1.2E−04	6052.7 ± 0.51	0.123 ± 0.004	0.1732 ± 8.4E−05	1	–	–
[Fe VI]	5176.4	6073.4 ± 0.66	0.097 ± 0.024	0.1733 ± 1.2E−04	6072.9 ± 0.60	0.094 ± 0.004	0.1732 ± 9.9E−05	4	1	–
[Fe IV]	5236.1	6142.3 ± 1.21	0.035 ± 0.005	0.1731 ± 2.1E−04	6143.3 ± 0.62	0.051 ± 0.006	0.1733 ± 1.0E−04	4	–	–
[Fe VII]	5276.4	6189.6 ± 0.65	0.121 ± 0.021	0.1731 ± 1.1E−04	6189.3 ± 0.52	0.113 ± 0.006	0.1730 ± 8.4E−05	1	–	–
[Ca V]	5309.1	6228.6 ± 0.70	0.135 ± 0.016	0.1732 ± 1.1E−04	6227.4 ± 2.10	0.105 ± 0.009	0.1730 ± 3.4E−04	1	–	–
[Fe VI]	5335.2	6259.9 ± 2.25	0.032 ± 0.005	0.1733 ± 3.0E−04	6259.7 ± 0.64	0.046 ± 0.007	0.1733 ± 1.0E−04	4	–	–
[Fe VI]	5425.7	–	–	–	6366.4 ± 0.64	0.030 ± 0.004	0.1734 ± 1.0E−04	6	–	–
[Fe VII]	5720.7	6712.0 ± 0.56	0.318 ± 0.027	0.1733 ± 1.0E−04	–	–	–	1	–	–
He I	5875.6	6893.1 ± 0.66	0.141 ± 0.026	0.1732 ± 1.0E−04	–	–	–	1	–	–
[Fe VII]	6086.9	7141.1 ± 0.52	0.495 ± 0.028	0.1732 ± 1.0E−04	–	–	–	1	–	–
[O I]	6300.3	7391.5 ± 0.55	0.196 ± 0.017	0.1732 ± 1.0E−04	–	–	–	1	–	–
[S III]	6312.1	7405.7 ± 0.55	0.060 ± 0.016	0.1733 ± 1.0E−04	–	–	–	1	–	–
[O I]	6363.8	7466.5 ± 0.55	0.063 ± 0.006	0.1733 ± 1.0E−04	–	–	–	1	–	–
[Fe X]	6374.6	7479.2 ± 0.55	0.234 ± 0.034	0.1733 ± 1.0E−04	–	–	–	1	–	–
[N II]	6548.1	7682.2 ± 0.61	0.262 ± 0.020	0.1732 ± 1.8E−04	–	–	–	1	–	–
Hα	6562.8	7699.5 ± 0.70	4.997 ± 0.173	0.1732 ± 1.9E−04	–	–	–	1	–	–
[N II]	6583.4	7723.6 ± 0.62	0.786 ± 0.059	0.1732 ± 1.8E−04	–	–	–	1	–	–
[S II]	6716.4	7879.7 ± 0.65	0.332 ± 0.039	0.1732 ± 1.0E−04	–	–	–	1	–	–
[S II]	6730.8	7896.1 ± 0.65	0.219 ± 0.039	0.1732 ± 1.0E−04	–	–	–	1	–	–
He I	7065.7	8290.0 ± 1.06	0.111 ± 0.024	0.1733 ± 1.3E−04	–	–	–	4	–	–
[Ar III]	7135.8	8371.0 ± 0.69	0.091 ± 0.031	0.1731 ± 1.0E−04	–	–	–	5	–	–
[O II]	7319.9	8586.3 ± 0.99	0.096 ± 0.028	0.1730 ± 1.3E−04	–	–	–	1	–	–
[O II]	7330.2	8598.3 ± 0.99	0.037 ± 0.011	0.1730 ± 1.3E−04	–	–	–	1	–	–
[Ar I]	7868.2	9228.6 ± 1.03	0.090 ± 0.022	0.1730 ± 1.3E−04	–	–	–	4	–	–
[Fe XI]	7891.8	9256.8 ± 0.67	0.157 ± 0.021	0.1730 ± 1.0E−04	–	–	–	1	–	–

Table 3. Unidentified emission lines across both spectra. The flux ratios are relative to Hβ. All presented wavelengths are measured in the observed frame. A notes key is included in Table 2.

λ_{WHT} (Å)	λ_{Gemini} (Å)	$(F/F)_{H\beta}$ (WHT)	$(F/F)_{H\beta}$ (Gemini)	Notes	Suggested ID
3344.0 ± 1.09	–	0.141 ± 0.034	–	2	[Ar IV]
3488.9 ± 0.91	–	0.055 ± 0.008	–	2	[Ne V]
3661.9 ± 0.52	3662.9 ± 0.61	0.072 ± 0.027	0.091 ± 0.007	2	[O III]
–	3747.9 ± 1.10	–	0.079 ± 0.009	–	?
3924.7 ± 0.51	3925.1 ± 0.52	0.420 ± 0.016	0.434 ± 0.034	–	O III/[Ne V]
–	3963.2 ± 0.56	–	0.023 ± 0.004	2	?
4040.4 ± 0.66	4039.4 ± 1.50	0.122 ± 0.033	0.099 ± 0.036	–	O III
–	4108.1 ± 1.50	–	0.029 ± 0.004	1	?
–	4174.6 ± 0.60	–	0.017 ± 0.002	2	?
4208.3 ± 0.51	4208.9 ± 0.58	0.164 ± 0.017	0.242 ± 0.012	–	[Fe VII]
–	4326.5 ± 0.52	–	0.006 ± 0.002	2	H I
–	4336.2 ± 0.52	–	0.008 ± 0.002	2	H I
4426.3 ± 1.24	4425.3 ± 1.45	0.010 ± 0.002	0.008 ± 0.001	–	H I
–	4438.4 ± 1.40	–	0.017 ± 0.004	2	?
–	4863.6 ± 0.60	–	0.034 ± 0.006	–	He I
–	4904.1 ± 0.52	–	0.040 ± 0.006	–	[Fe V]
–	4933.8 ± 0.70	–	0.030 ± 0.006	–	?
4979.8 ± 0.57	4979.7 ± 0.55	0.091 ± 0.022	0.080 ± 0.009	–	?
5030.2 ± 1.13	5029.6 ± 0.66	0.072 ± 0.027	0.047 ± 0.014	–	?
–	5066.6 ± 0.50	–	0.056 ± 0.007	–	[O II]
–	5291.0 ± 2.40	–	0.009 ± 0.002	–	[N III]
5301.8 ± 0.59	5302.1 ± 1.60	0.056 ± 0.027	0.030 ± 0.004	1	?
–	5443.5 ± 1.10	–	0.024 ± 0.006	–	[N III]
–	5544.5 ± 0.76	–	0.048 ± 0.009	–	?
–	5561.1 ± 0.63	–	0.045 ± 0.009	–	?
–	5649.8 ± 0.52	–	0.034 ± 0.006	–	?
–	5915.6 ± 0.60	–	0.025 ± 0.006	1	[Si II]
–	6122.5 ± 0.60	–	0.010 ± 0.002	2	?
–	6171.4 ± 0.81	–	0.018 ± 0.004	–	?
–	6238.3 ± 5.90	–	0.025 ± 0.007	–	?
–	6309.3 ± 0.78	–	0.029 ± 0.006	–	?
–	6350.1 ± 0.52	–	0.036 ± 0.004	–	He II
6481.8 ± 1.42	–	0.023 ± 0.003	–	–	?
6495.8 ± 1.15	–	0.044 ± 0.019	–	–	?
6588.3 ± 2.17	–	0.024 ± 0.008	–	–	?
6605.3 ± 2.18	–	0.239 ± 0.016	–	–	[Fe VI]
6748.5 ± 2.94	–	0.046 ± 0.010	–	2	[N II]
8403.8 ± 3.14	–	0.062 ± 0.013	–	–	?

is identified with [Fe XIV] λ5303, the individual redshift becomes 0.174 55 ± 0.000 11, which is significantly higher ($>10\sigma$) than the mean redshift.

A further interesting feature of the spectrum is that the Hα +[N II] emission blend shows tentative evidence for a broad base of the rest-frame width 11 500 ± 2200 km s^{-1} (FWHM, see Figs 4 and 6). This is consistent with the presence of a scattered (Antonucci & Miller 1985), or directly observed, BLR component. Spectropolarimetry observations will be required to confirm the scattered BLR possibility.

3.3 Infrared spectrum

In order to further understand the nature of this object, we made spectroscopic observations of Q1131+16 at near-IR wavelengths. The observed wavelength range (1.4–2.4 µm) was selected in order to simultaneously detect both Paα and Paβ.

The K-band near-IR spectrum of Q1131+16 taken using the LIRIS is presented in Fig. 7. Due to its relatively low S/N, this spectrum does not show the abundance of emission lines seen at optical wavelengths. Although weak narrow Paα and Paβ[4] emission lines are detected, there is no sign of any broad Paα and Paβ components, implying that the BLR is enshrouded by dust. A single-Gaussian fit to the Paα line shows that it is unresolved within the uncertainties for the resolution of our observations, and its redshift ($z = 0.173\,14 \pm 0.000\,11$) is consistent with those of the optical emission lines.

Any quasar nucleus component present in this system must be highly extinguished; the relatively red near-IR colours of this source measured by the 2MASS do not appear to be due to a moderately extinguished quasar component that becomes visible at the longer near-IR wavelengths. Therefore, this object cannot truly be described as a 'red quasar'.

3.4 Spectral fitting model

The emission lines in the spectrum of Q1131+16 were initially fitted with single-Gaussian profiles, but such fits did not provide an

---

[4] The Paβ emission line is on the blue edge of the H-band near-IR spectrum; because of this any measured emission-line fluxes are inaccurate.
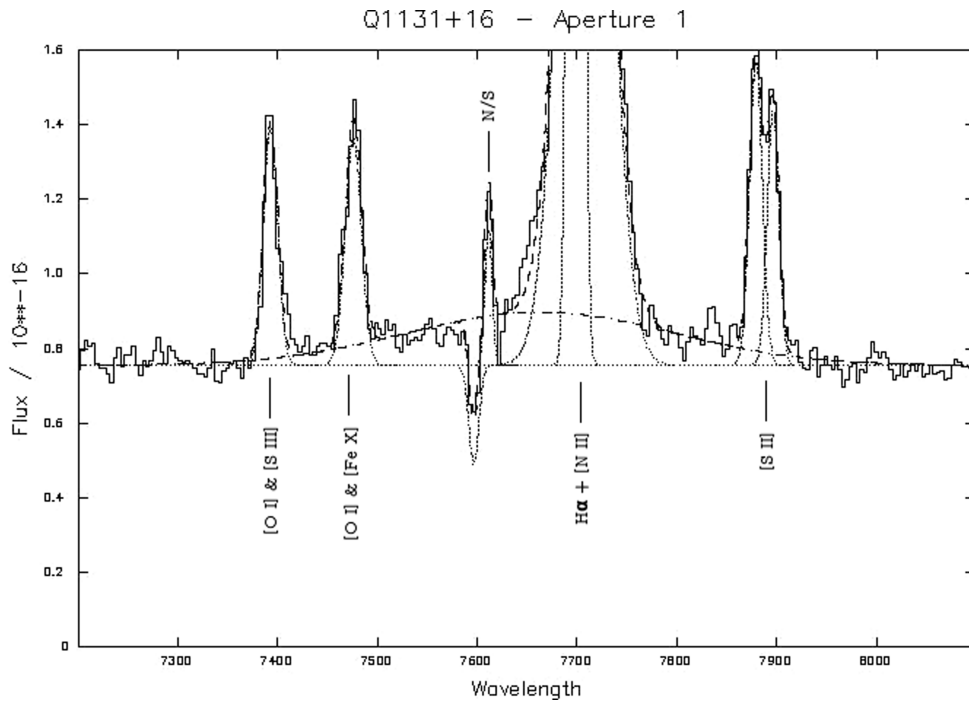
Q1131+16 — Aperture 1

Figure 6. The broad component centred on the Hα +[N ɪɪ] emission blend. The telluric feature is fitted as well as the various emission components from Q1131+16.
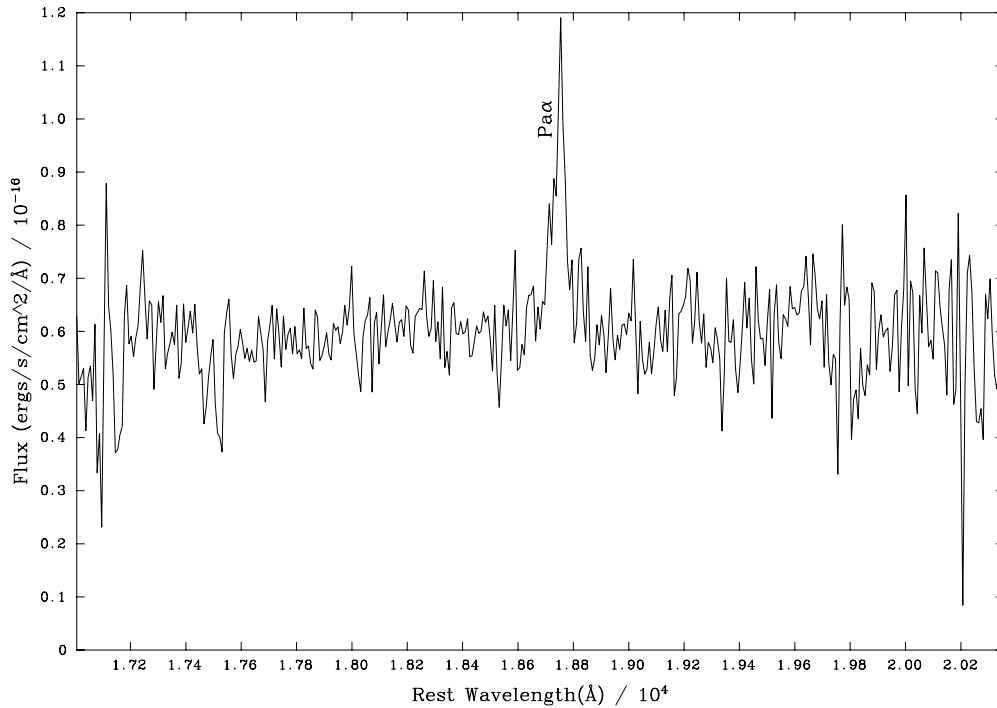

Figure 7. The *K*-band LIRIS spectrum of Q1131+16. The rest-wavelength range shown here is 17 000–20 500 Å. The only significant feature is the Paα emission line.

entirely adequate fit to the wings of the stronger lines (see Fig. 8). To overcome this, a double-Gaussian model was fitted to the spectral lines. This model is based on the fit of the [O ɪɪɪ] λλ5007,4959 lines, because they are particularly strong emission features. To produce the model, both broad and narrow Gaussians were fitted to the Gemini [O ɪɪɪ] line profiles, where the centres, widths and intensities of each Gaussian were free parameters. The widths (FWHMs) of the narrow components for the [O ɪɪɪ] emission lines were found to be consistent with the instrumental width of the Gemini spectra (7.1 Å) at 6.9 ± 0.2 Å. We therefore use the instrumental width to fit the narrow components in the model fit to other lines, varying this to take into account the resolution of the different spectra. The measured
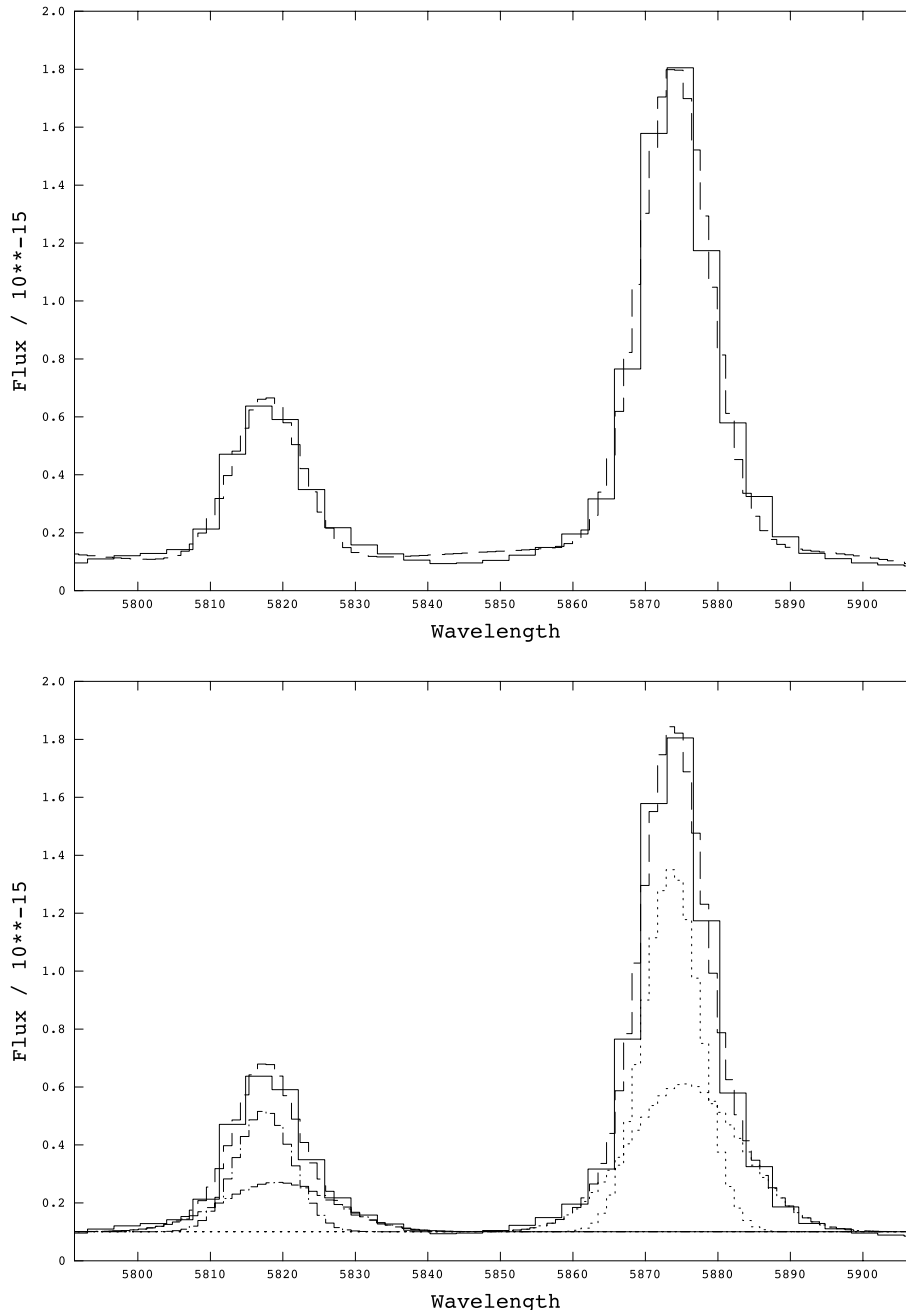
Figure 8. Fits to the [O III] $\lambda\lambda 5007,4959$ emission lines. Top panel: single-Gaussian fit to both [O III] $\lambda 5007$ and [O III] $\lambda 4959$. The overall fit does not fit the wings of the emission lines well. Bottom panel: the double-Gaussian fit to the [O III] $\lambda 5007$ and [O III] $\lambda 4959$ emission lines from the Gemini data. Here the model has had more success in fitting the wings of the emission lines when compared to that above. The individual components of the fit are included in the plot; the components of [O III] $\lambda 5007$ are drawn with a dotted line and the components of $\lambda 4959$ are fitted with a dot and a dashed line. The overall line profile is fitted with a dashed line. The model throughout this investigation is based on the [O III] $\lambda 5007$ emission line. The flux is measured in 10^{-15} erg s^{-1} Å^{-1} cm^{-2} and the wavelength is in units of Å.

FWHM of the broad component [14.1 $\pm$ 0.6 Å (FWHM), corresponding to a rest-frame velocity width of 720 $\pm$ 30 km s^{-1}] was used to obtain an intrinsic velocity width for the broader component by correcting its FWHM in quadrature using the instrumental width. In addition, the broad component is redshifted by 1.8 $\pm$ 0.1 Å from the narrow component, corresponding to a velocity shift of 92 $\pm$ 6 km s^{-1} in the galaxy rest frame. The double-Gaussian [O III] model was then fitted to all other emission lines, in order to derive the line fluxes listed in Tables 2 and 3.

Fig. 8 shows the spectral fit to the [O III] $\lambda 5007$ emission line used to determine the spectral fitting model. The overall fit in the bottom panel of Fig. 8 is significantly better than that shown in the top panel, where the emission lines are fitted with a single-component free fit. The parameters from the double-Gaussian [O III] fits were used to fit the emission lines throughout the spectrum. In general, these fits were extremely successful. There is, however, a minority of lines – indicated by notes (1) and (2) in Tables 2 and 3 – which are not fitted well by both components of the [O III] model. These lines
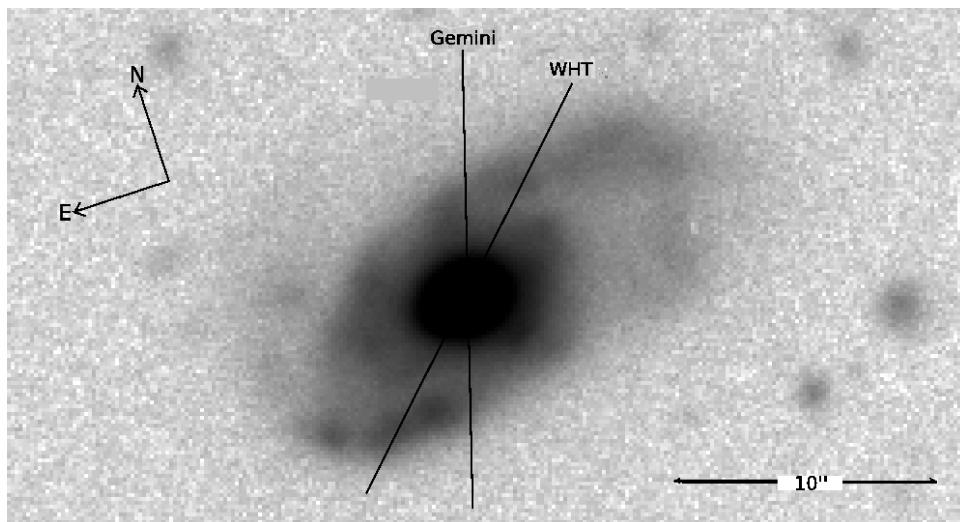
Figure 9. GMOS r' image of the host galaxy Q1131+16. Indicated are the north and east axes as well as the slit PA of each spectroscopic data set.

are generally weak, and many are in blends with other emission lines.

The [N II] $\lambda\lambda6548,6584$ doublet is blended with the Hα emission line and therefore was modelled using constraints provided by atomic physics (i.e. same FWHM, 1:3 intensity ratio and line centre of $\lambda6548$ fixed to the centre of $\lambda6583$). This is true of other doublet blends, for example, [O I] $\lambda\lambda6300,6364$ (blended with [S III] $\lambda6312$ and [Fe X] $\lambda6375$).

3.5 Host galaxy morphology

Fig. 9 presents our Gemini r'-band image of Q1131+16. The galaxy morphology appears consistent with a late-type spiral classification (Sb or Sc), with a moderate degree of asymmetry in the sense that the spiral arms are more extended to the west than to the east of the nucleus. However, we do not find evidence for the 'large-scale and clear tidal disturbance' reported by Hutchings et al. (2003). Clearly, a more detailed analysis of the morphology and kinematics of the host galaxy is required in order to determine the true interaction status of this system.

Based on aperture photometry, the total magnitude of the host galaxy was estimated using a circular aperture of diameter 23 arcsec (57 kpc), giving an r'-band magnitude of 17.11 ± 0.26 – consistent with the Petrosian r-band magnitude for this object listed on the SDSS website. Note that this estimate represents an upper limit on the brightness of the stellar component of the host galaxy since no correction has been made for AGN components, such as emission lines and scattered light.

3.6 Emission-line kinematics and redshift

The median redshift determined using all of the securely identified emission lines is $z = 0.173\,25 \pm 0.000\,01$. From only the securely identified FHILs (ionization potential ≥ 54.4 eV) the redshift is $z = 0.173\,23 \pm 0.000\,02$, while for the low-ionization lines, we find $z = 0.173\,26 \pm 0.000\,01$. These values are consistent within their uncertainties, as emphasized by Fig. 10, where estimated redshifts of all the lines are plotted.

In order to check whether the mean emission-line redshift represents that of the host, the [O II] $\lambda3727$ emission-line blend was fitted as a function of position across the galaxy for both Gemini and WHT
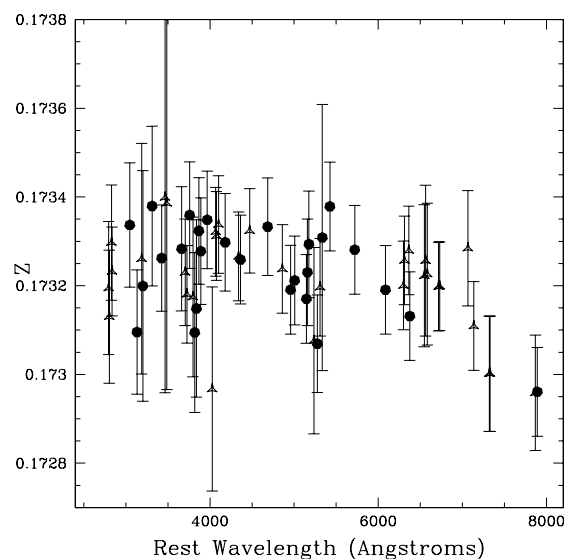

Figure 10. Individual redshifts of the emission lines of Q1131+16 as measured for the WHT data. The triangles indicate the low-ionization emission lines and neutral species emission and the black circles indicate the FHILs. All points lie within 1.5σ of the mean redshift; however, the longer wavelength emission lines ([O II] $\lambda\lambda7320,7330$, [Ar IV] $\lambda7868$ and [Fe XI] $\lambda7892$) do not. This is likely due to larger wavelength calibration errors at the long-wavelength end of the spectrum.

spectra. Fig. 11 presents the results. The velocities were determined relative to the median redshift of all the emission lines of the system ($z = 0.173\,25 \pm 0.000\,01$), assuming a rest-frame wavelength of 3727.4 Å for the blend – representing the flux-weighted wavelength of the [O II] $\lambda\lambda3726,3729$ blend for a density of 10^3 cm^{-3}. For both PAs, the central region (±1.2 arcsec, ±4 kpc) shows a velocity field that resembles a rotation curve; the velocity gradient of the [O II] $\lambda3727$ emission in the nucleus can also be clearly seen in Fig. 1. This component of emission may correspond to an inner disc of the galaxy, implying that the [O II] $\lambda3727$ emission component in Q1131+16 is resolved in the nucleus. However, the two data sets differ significantly at larger radii; such differences are likely due to the different slit PAs, given that each slit intersects different regions of Q1131+16 (see Fig. 9): while the slit for the Gemini data is
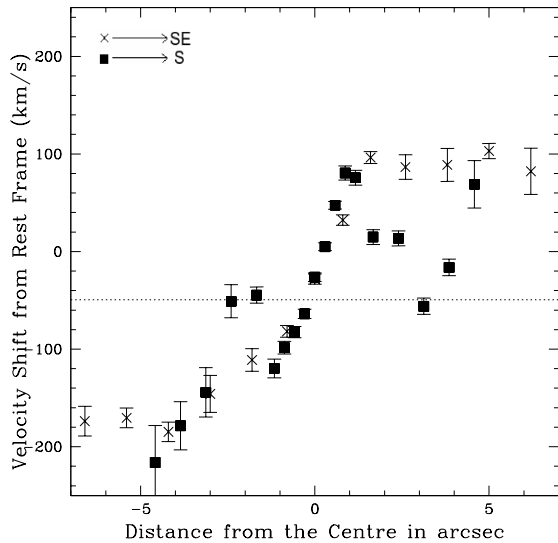
Figure 11. The rotation curves for Q1131+16. The crosses (WHT, PA = 315°) and filled squares (Gemini, PA = 163°) are the measured velocity shifts determined at different spatial locations along the slit of the long-slit spectrum. The directions of the slits are indicated in the upper left-hand corner. Velocity shifts are determined from the difference between the measured redshift of [O II] on each pixel and the average redshift of the emission lines. The horizontal line indicates the bisector of the flat parts of the rotation curves at large radii along PA = 315°.

within $\sim 20°$ of the minor-axis of the host galaxy, that for the WHT is offset for the minor-axis by $\sim 50°$.

The rotation curve derived from the PA = 315° WHT data appears flat at large radii. However, the velocities of the flat parts of the velocity curves are asymmetric about the host redshift measured from the nuclear spectrum: the rotation velocity ranges from $+90 \pm 5 \, \mathrm{km \, s^{-1}}$ for the region moving away from the observer to $-176 \pm 5 \, \mathrm{km \, s^{-1}}$ for the region moving towards the observer in the WHT spectrum. This asymmetry can be explained by either the uncertainty in the electron density assumed in determining the rest wavelength of the [O II] blend (n_e is likely to differ between the nucleus and the disc of Q1131+16), or the uncertainty in the wavelength calibration of the spectrum. Both of these aspects can systematically shift the curve in Fig. 11, leading to an asymmetric appearance. However, despite the apparent asymmetry, the bisector of the two flat parts of the rotation curve is within $50 \, \mathrm{km \, s^{-1}}$ of the rest frame of the host galaxy estimated on the basis of the median redshift derived from the nuclear spectrum. Thus, our data provide no evidence for high-velocity outflows in the nuclear emission-line regions.

On the other hand, the rotation curve derived from the PA = 163° Gemini data appears more complex: outside the inner rapidly rotating region, the velocities drop significantly at intermediate radii ($1.2 < r < 2.5$ arcsec) on either side of the nucleus, before rising again at larger radii. It is possible that the inner rapid rotation along PA = 163° samples the seeing disc of the same inner disc component detected in the WHT data along PA = 315°. In this case, the initial drop in the velocities ($1.2 < r < 2.5$ arcsec) may be due to the slit sampling the outer disc close to the minor-axis where the (projected) rotation velocity amplitude is likely to be small. However, given the complexity of the rotation curve along PA = 163°, non-circular gas motions cannot be ruled out.

Our double-Gaussian [O III] model fits the majority of the lines well in the nuclear spectrum, suggesting that the velocity widths of
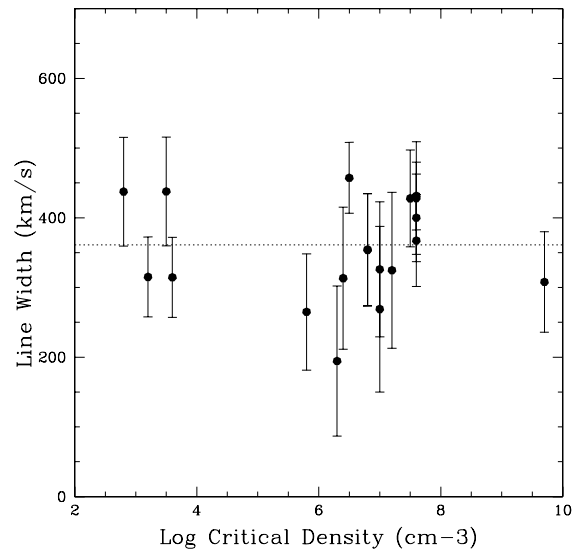

Figure 12. Rest-frame linewidth (FWHM) versus critical density for the emission lines of Q1131+16. The linewidths have been determined from single-Gaussian free fits to the emission lines and have been corrected for the instrumental profile.
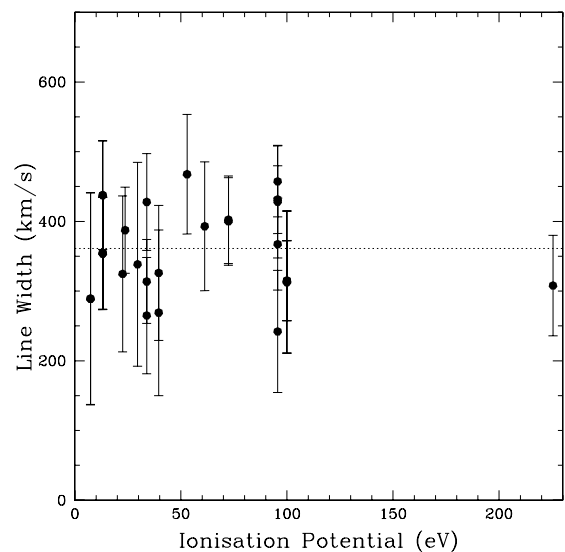

Figure 13. Rest-frame linewidth (FWHM) versus ionization potential for the emission lines of Q1131+16. The linewidths have been determined from single-Gaussian free fits to the emission lines and have been corrected for the instrumental width.

the FHIL and low-ionization emission lines are similar. The median rest-frame velocity width of the emission lines, based on single-Gaussian fits, is found to be $361 \pm 29 \, \mathrm{km \, s^{-1}}$ (FWHM).

Figs 12 and 13 also show that there is no correlation between the widths of the emission lines as measured by single-Gaussian fits and their critical densities and ionization potentials. Again this suggests that the kinematics of the FHILs and the low-ionization lines are similar.

3.7 FHILs in 'typical' Seyfert galaxies

FHILs are detected in the spectra of all types of Seyfert galaxies (Penston et al. 1984). These emission lines have been studied rigorously in the past (e.g. Penston et al. 1984; Nagao, Taniguchi

Table 4. Line flux ratios for Balmer recombination emission lines for both the WHT and the Gemini observations. Ratios are relative to Hβ. The last three columns in the table are the expected ratios for Case B recombination at different temperatures at a typical NLR density (10^4 cm^{-3}, Osterbrock 1978).

Species	WHT	Gemini	10 000 K	20 000 K
Hα	4.99 ± 0.17	–	2.85	2.74
Hγ	0.44 ± 0.02	0.45 ± 0.03	0.47	0.48
Hδ	0.24 ± 0.02	0.24 ± 0.01	0.26	0.26

& Murayama 2000; Mullaney & Ward 2008) and several common properties have been identified. It is therefore important to highlight the differences between the spectrum of Q1131+16 and the spectra of 'typical' Seyfert galaxies.

One of the most notable features of the FHILs in typical AGNs is that the velocity widths (FWHMs as measured by single-Gaussian fits) tend to be intermediate between those of the NLR and BLR (in the range of $500 < \text{FWHM} < 1000 \, \text{km s}^{-1}$, Appenzeller & Östreicher 1991). However, the FHILs in Q1131+16 and other similar objects (e.g. III Zw 77, Tololo 0109-383, etc.) do not share this property. In the case of Q1131+16, Figs 12 and 13 show no significant variation in the velocity width (FWHM) with the critical density and ionization potential.

For typical AGNs, it is also found that FHILs are blueshifted with respect to the host galaxy rest frames. In fact, the blueshift correlates with the observed velocity FWHM (Mullaney et al. 2009). There is no evidence for this in the spectrum of Q1131+16. The individual redshifts from single-Gaussian fits of each emission line are plotted in Fig. 10. From this it is clear that there is no tendency for the FHILs to be blueshifted with respect to the average redshift of the low-ionization lines; the points representing the FHIL redshifts are scattered about the average redshift of the low-ionization species.

Finally, the FHILs of Q1131+16 and similar objects have larger EWs when compared with those of other 'typical' Seyfert galaxies.

3.8 Balmer decrements

In order to derive accurate physical conditions, it is important to correct for any intrinsic dust extinction. The most common way to achieve this for optical spectra is to use Balmer line recombination ratios.

Table 4 presents flux ratios for the Balmer recombination lines measured from the Gemini and WHT spectra. The Hγ/Hβ and Hδ/Hβ ratios in both spectra agree with their theoretical Case B values within the uncertainties, assuming conditions typical of the NLR. This suggests that there is no need for an extinction correction for the spectrum of Q1131+16. Note that, because of the large EWs of the Balmer lines, uncertainties due to underlying Balmer absorption lines from young stellar populations in the host galaxy are not a serious issue for Q1131+16.

Another interesting feature of the spectrum of Q1131+16 is that its Hα flux is high when compared to other Balmer lines in the series. The Hα/Hβ ratio is not consistent with Case B recombination (Hα/Hβ = 4.99 ± 0.17) (see Section 4.2 for a detailed discussion). Given the potential for the collisional excitation of the Hα line (see Section 4.2; Gaskell & Ferland 1984), we ignore the Hα/Hβ ratio when assessing the level of extinction in Q1131+16. Therefore, since the high-order Balmer line ratios for this source provide no evidence for significant reddening, we make no reddening correction of the line ratios.

Table 5. Diagnostic line intensity ratios measured for the nuclear regions of Q1131+16, as derived from the WHT data. The values in brackets are the ratios given by the Gemini data. Potentially, the [Fe VII] λ6086 line may suffer from some contamination by [Ca V] λ6087. However, the fact that the [Fe VII] (5720/6086) ratio is within 1σ of the value predicted by atomic physics ([Fe VII (5720/6086) = 0.617: Nussbaumer & Storey 1982) indicates that any such contamination is modest.

Species	Ratio	$\pm$
[O II] (3726+3729)/(7317+7330)	5.02	1.19
[O III] (5007/4363)	5.86(6.84)	0.21(0.32)
[O III] (5007/Hβ)	5.27(5.74)	0.16(0.16)
[S II] (6717+6731)/(4069+4076)	7.51	1.46
[Fe VI] (5176)/[Fe V] (3891)	0.267(0.176)	0.076(0.008)
[Fe VII] (6086/3759)	1.18	0.076
[Fe VII] (5159/6086)	0.208	0.067
[Fe VII] (5720/6086)	0.667	0.067
[Fe X] (6375)/[Fe VII] (6086)	0.473	0.074
[Fe XI] (7892)/[Fe VII] (6086)	0.317	0.046
[Ne V] (3426)/[Fe VII] (6086)	2.04	0.207

4 DISCUSSION

4.1 Physical conditions implied by the FHILs

To investigate the physical conditions implied by both the low- and high-ionization species, the photoionization model code CLOUDY[5] (Ferland 1998) was used to create single-slab photoionization models for the emission lines of Q1131+16. The ionization parameter was varied over the range $-3.0 \leq \log[U] \leq 0$, in steps of $\log[U] = 0.5$, and the hydrogen density was varied over the range $3.0 \leq \log(n_\text{H}/\text{cm}^{-3}) \leq 8.0$ in steps of $\log(n_\text{H}/\text{cm}^{-3}) = 0.5$. The rest of the properties of the model were kept constant: an ionizing continuum power-law index of -1.2 was assumed,[6] and we only considered radiation-bounded models that are optically thick to the ionizing continuum. In terms of abundances, Solar 84 was used (see Grevesse & Anders 1989; Grevesse & Noels 1993). Also no grains were included. This was so that the CLOUDY results were not affected by the depletion of iron due to condensation on to dust grains. Nagao et al. (2003) have demonstrated for a large sample of AGNs that the observed FHIL ratios[7] cannot be reproduced in CLOUDY models that contain grains, but can be successfully reproduced with models not containing grains.

The ratios measured for each of the main diagnostic ratios used in this study are given in Table 5. The WHT ratios are used in this investigation because the WHT spectrum has the greatest wavelength range.

Considering first the low-ionization lines, we plot the transauroral [O II] (3726+3729)/(7317+7330) and [S II] (6717+6731)/ (4069+4076) ratios against each other in Fig. 14. By comparison with the models, the ratios are consistent with hydrogen densities in the range $3.5 < \log(n_\text{H}/\text{cm}^{-3}) < 4.5$ and ionization parameters $-3.0 < \log[U] < -2.0$. The densities and ionization parameters found for these low-ionization ratios are typical of those found for the NLR of AGNs in general (e.g. see Peterson 1997; Osterbrock & Ferland 2006).

---

[5] The version of CLOUDY used in this investigation is c08.00.
[6] When testing power laws between -1.5 and -0.8, this power law was found to be the most successful at modelling the observed He II λ4686/Hβ ratio compared to the FHIL ratios.
[7] The ratio used in Nagao et al. (2003) was [Fe VII] λ6086/[Ne V] λ3426.
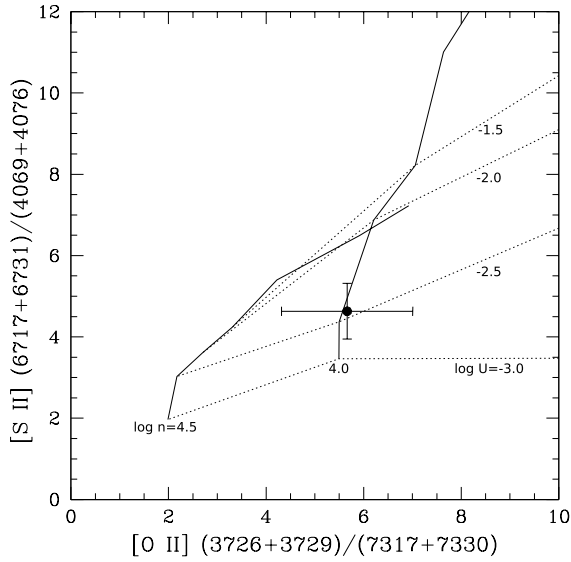
Figure 14. Diagnostic plot showing the measured [S II] (6717+6731)/ (4069+4076) and [O II] (3726+3729)/(7317+7330) transauroral ratios (filled point), compared with photoionization model results for different densities and ionization parameters. Equal densities are connected by the solid lines (as labelled) and the ionization parameters are connected by the dotted lines (as labelled).
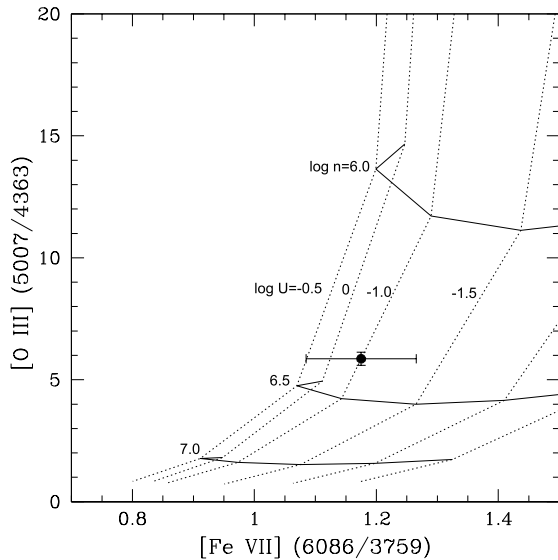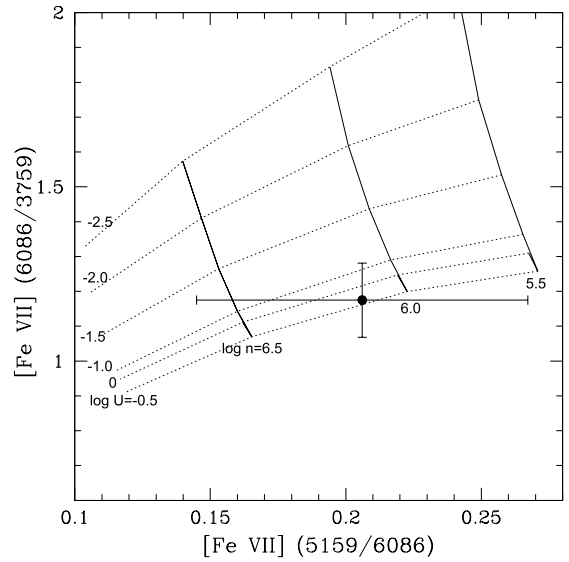

Figure 16. Diagnostic plot showing the measured [Fe VII] (6086/3759) and [Fe VII] (5159/6086) ratios (filled point), compared with photoionization model results for different densities and ionization parameters. Equal densities are connected by the solid lines (as labelled) and the ionization parameters are connected by the dotted lines (as labelled).
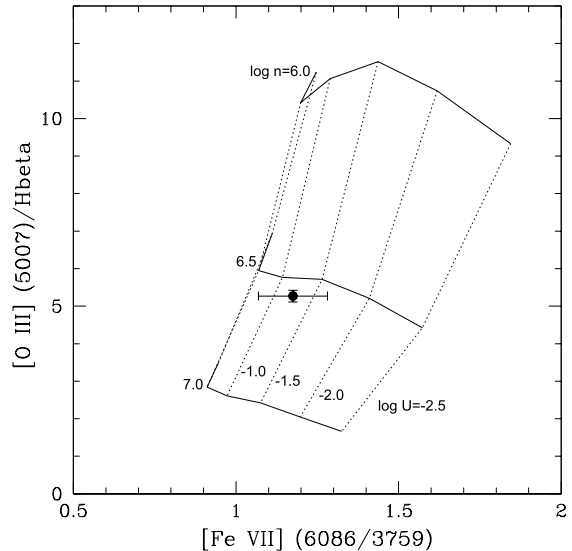

Figure 15. Diagnostic plot showing the measured [O III] (5007/4363) and [Fe VII] (6086/3759) ratios (filled point), compared with photoionization model results for different densities and ionization parameters. Equal densities are connected by the solid lines (as labelled) and the ionization parameters are connected by the dotted lines (as labelled).

Figure 17. Diagnostic plot showing the measured [O III] $\lambda 5007$/Hβ and [Fe VII] (6086/3759) ratios (filled point), compared with photoionization model results for different densities and ionization parameters. Equal densities are connected by the solid lines (as labelled) and the ionization parameters are connected by the dotted lines (also labelled).

the latter ratios are much higher than those implied by the low-ionization emission lines.

As mentioned previously, the [O III] $\lambda 5007$ emission-line intensity is surprisingly low relative to Hβ for an AGN with a high-ionization emission-line spectrum. Fig. 17 illustrates that such a low ratio is possible at high densities. The [O III] $\lambda 5007$/Hβ emission ratio is consistent with hydrogen densities $6.5 < \log(n_H/\text{cm}^{-3}) < 7.0$ and ionization parameters in the range $-1.5 < \log[U] < 0$. At such densities, above the critical densities of the [O III] $\lambda\lambda 5007,4959$ transitions, the [O III] emission lines are suppressed relative to Hβ; this explains the relatively low [O III] $\lambda 5007$/Hβ ratio.

On the other hand, the high-ionization species show markedly different results. In Fig. 15, the [Fe VII] (6086/3759) ratio is plotted against the [O III] (5007/4363) ratio. These ratios are consistent with hydrogen densities $6.0 < \log(n_H/\text{cm}^{-3}) < 6.5$ and ionization parameters in the range $-1.5 < \log[U] < 0$. Similarly, Fig. 16 shows the results found by comparing the [Fe VII] ratios of (6086/3759) and (5159/6086). These ratios are consistent with hydrogen densities $5.5 < \log(n_H/\text{cm}^{-3}) < 7.0$ and ionization parameters $-1.0 < \log[U] < 0$. The densities and ionization parameters indicated by
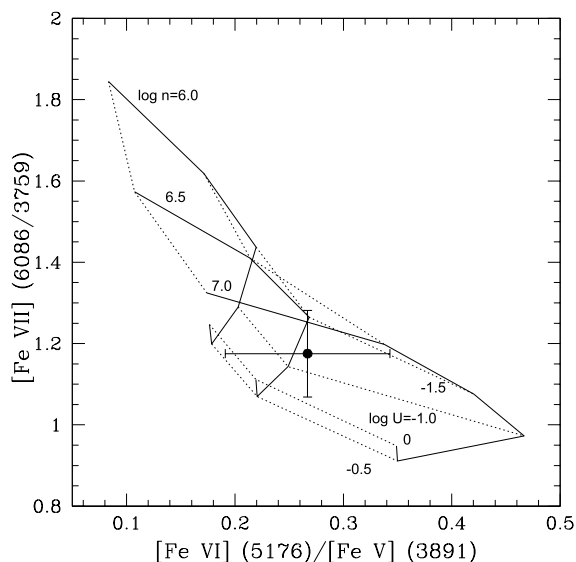
Figure 18. Diagnostic plot showing the measured [Fe VII] (6086/3759) and [Fe VI] λ5176/[Fe V] λ3891 ratios (filled point), compared with photoionization model results for different densities and ionization parameters. Equal densities are connected by the solid lines (as labelled) and the ionization parameters are connected by the dotted lines (as labelled).
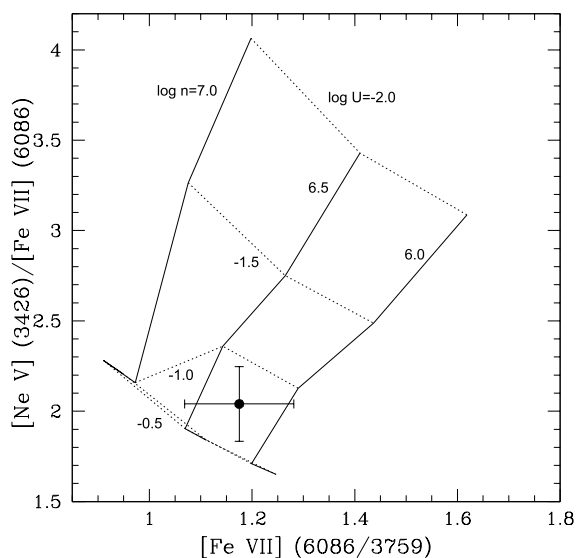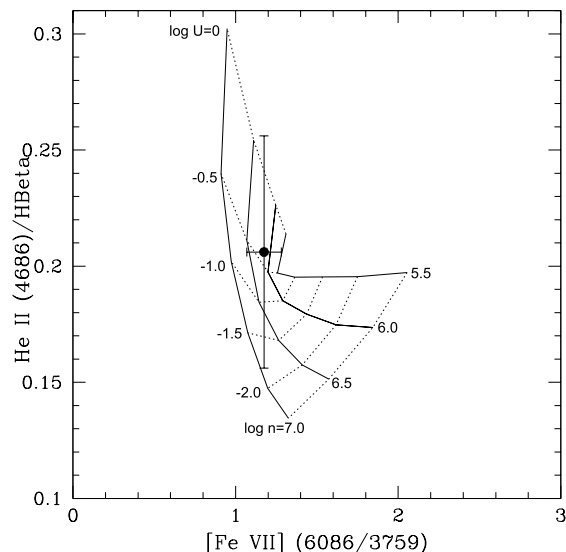

Figure 20. Diagnostic plot showing the measured He II λ4686/Hβ and [Fe VII] (6086/3759) ratios (filled point), compared with photoionization model results for different densities and ionization parameters. Equal densities are connected by the solid lines (as labelled) and the ionization parameters are connected by the dotted lines (as labelled).

Figure 19. Diagnostic plot showing the measured [Ne V] λ3426/Hβ and [Fe VII] (6086/3759) ratios (filled point), compared with photoionization model results for different densities and ionization parameters. Equal densities are connected by the solid lines (as labelled) and the ionization parameters are connected by the dotted lines (as labelled).

FHILs with lower ionization potentials, such as [Fe VI] λ5176, are also consistent with the results found using the [Fe VII] ratios. In Fig. 18, the [Fe VII] (6086/3759) ratio is plotted against the [Fe VI] λ5176/[Fe V] λ3891 ratio. These ratios are consistent with hydrogen densities $6.5 < \log(n_H/\mathrm{cm}^{-3}) < 7.0$ and ionization parameters in the range $-1.5 < \log[U] < 0$.

Similarly, FHILs which are not from iron ions are consistent with the results found using the [Fe VII] ratios. Fig. 19 shows the [Ne V] λ3426/[Fe VII] λ6086 ratio plotted against the [Fe VII] (6086/3759) ratio. This diagram is consistent with hydrogen densities $5.5 < \log(n_H/\mathrm{cm}^{-3}) < 6.5$ and ionization parameters $-1.0 < \log[U] <$

-0.5. Therefore, the high densities and ionization parameters found for the FHILs are not limited to iron ions.

The He II λ4686/Hβ ratio is relatively insensitive to the density of the emission region, but more sensitive to the shape of the ionizing continuum spectrum (e.g. Penston & Fosbury 1978), and whether the emitting regions are matter bounded (Robinson et al. 1987). Therefore, this ratio can be used to check whether the emission clouds are radiation bounded 'as assumed' and also whether the assumed ionizing continuum shape is appropriate. The measured He II λ4686/Hβ ratio is found to be 0.21 ± 0.05 and 0.23 ± 0.01 for the WHT and Gemini spectra, respectively. Fig. 20 shows this ratio plotted against the [Fe VII] (6086/3759) ratio. The densities and ionization parameters implied by this diagram are consistent with those deduced from other diagnostic diagrams involving the FHILs [$5.0 < \log(n_H/\mathrm{cm}^{-3}) < 7.0$, $-1.5 < \log[U] < 0$]. In this case, the consistency between the data and the models, as well as the results for other high-ionization line ratios, supports the assumption of optically thick models with an ionizing continuum spectral index of -1.2.

Although the models can successfully reproduce the FHIL line ratios in Table 5, the emission-line ratios involving lines with the highest critical densities (e.g. Hα/Hβ, [Fe X]/[Fe VII]) cannot be successfully modelled using the range of physical conditions and ionization parameters that successfully reproduce the [Fe VII] and [O III] line ratios. Indeed, the higher critical density line ratios can only be reproduced at higher densities ($n_H > 10^7 \mathrm{cm}^{-3}$) using CLOUDY. Fig. 21 shows the Hα/Hβ ratio plotted against the [Fe X] λ6374/[Fe VII] λ6086 ratio. In this case, hydrogen densities of $7.5 < \log(n_H/\mathrm{cm}^{-3}) < 8.0$ and ionization parameters $-1.5 < \log[U] < -1.0$ are required to reproduce the data. This suggests that some regions in Q1131+16 have even higher densities than implied by the [Fe VII], [Fe VI] and [O III] diagnostic ratios.

To summarize, most of the key high- and low-ionization diagnostic ratios are consistent with the radiation-bounded photoionization models. While the low-ionization lines require low densities [$3.5 < \log(n_H/\mathrm{cm}^{-3}) < 4.5$] and ionization parameters

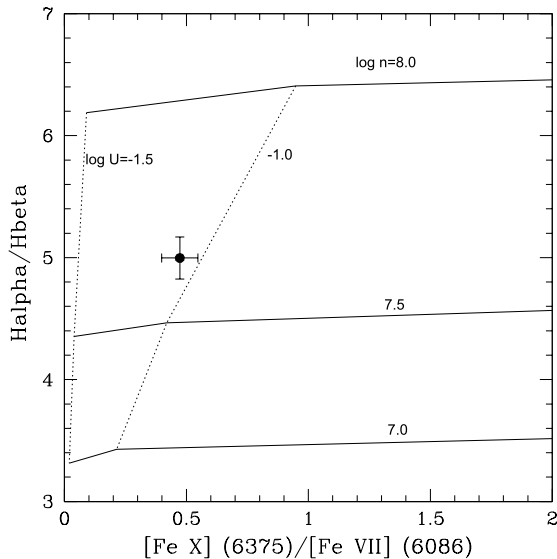**Figure 21.** Diagnostic plot showing the measured Hα/Hβ and [Fe x] λ6374/[Fe vii] λ6086 ratios (filled point), compared with photoionization model results for different densities and ionization parameters. Equal densities are connected by the solid lines (as labelled) and the ionization parameters are connected by the dotted lines (also labelled).

$(-3.0 < \log[U] < -2.0)$, the higher ionization lines imply much higher densities $[6.0 < \log(n_H/cm^{-3}) < 8.0]$ and ionization parameters $(-1.5 < \log[U] < 0)$. However, it is important to emphasize that our approach assumes that the lines contributing to a particular ratio are emitted by a single cloud with a single density and ionization parameter; the reality is likely to be more complex. In particular, some of the low-ionization lines (e.g. [S ii] λ4072, [O ii] λ7330) may have contributions from the high-density/high-ionization regions, while some of the higher ionization lines (e.g. [O iii] λ5007, Hβ) will have contributions from the low-density/low-ionization region. Therefore, the differences deduced between the conditions in the high- and low-density regions may be even more extreme than implied by our simple analysis.

4.2 Explaining the high Hα/Hβ ratio

The Hα/Hβ ratio gives an unusual result in Q1131+16. This may be due to the high density of the FHIL region in this object coupled with an extended partially ionized zone (Gaskell & Ferland 1984). Such high densities can lead to significant collisional excitation of the neutral hydrogen atoms in the partially ionized zones of clouds in the FHIL region. This results in an enhanced Hα emission, but no further enhancement in the other Balmer series emission lines, which have lower cross-sections for collision, as well as higher excitation temperatures (Gaskell & Ferland 1984; Osterbrock & Ferland 2006). Such a process could explain the high Hα/Hβ ratio measured in the spectrum of Q1131+16, since there is likely to be a major contribution from the FHIL region to the line flux of Hα.

The Hα/Hβ flux ratio was investigated using CLOUDY, as described in Section 4.1. The ratio indicated by the WHT data could only be reached at the highest densities ($n_H > 10^7$ cm^{-3}: see Fig. 21) and is not consistent with the conditions implied by the [Fe vii] and lower iron species ratios. Note that high Hα/Hβ ratios would also be favoured by lower metal abundances and a harder ionizing continuum than we have assumed in our modelling (Gaskell & Ferland 1984).

4.3 Location of the FHIL region

The presence of FHILs in the spectra of the majority of active galaxies has led to a number of studies on their nature, kinematics and location in AGNs (e.g. see Mullaney et al. 2009). One of the most credible suggestions for the origin of the FHIL emission is the inner torus wall (see Murayama & Taniguchi 1998 and Nagao et al. 2001). The FHIL emission is rich in iron lines, which can be enhanced (relative to the classical NLR) by the evaporation of dust grains in the inner torus wall, releasing the iron locked up in the grains (Pier & Voit 1995). Moreover, studies of the molecular emission from the circumnuclear molecular clouds of the centres of the Milky Way and other galaxies (hypothetically the torus) reveal densities in the range $n_{H_2} \sim 10^5$–10^6 cm^{-3} (e.g. Paglione et al. 1998), similar to the densities deduced for the FHILs.

In the case of Q1131+16, our results are consistent with the idea that the FHILs are emitted by the *far wall* of the torus, observed with our line of sight at a relatively large angle to the torus axis. We emphasize that such a geometry is consistent with the relatively narrow linewidths and small velocity shifts of the FHIL, since the circular velocities associated with the torus, and any out-of-the-plane gas motions, would then be directed close to perpendicular to the line of sight. In this case, our results imply that the torus is dynamically cold, with velocity dispersion that is small relative to its circular velocity.

It is difficult to entirely rule out the idea that the FHILs are emitted by an infalling molecular cloud or a clump of the torus which has broken off from the rest of the torus and is falling towards the AGN. However, in such cases, we might expect to see a larger velocity shift between the FHIL emission lines and the host galaxy rest frame, unless the cloud happens to be falling perpendicular to the line of sight.

Therefore, the FHIL emission is most likely to originate from the inner torus wall of the AGN, supporting the original suggestion of Murayama & Taniguchi (1998) and Nagao et al. (2001).

4.4 The radial distance to the FHIL region

The idea that the FHIL region is located in the torus can be further investigated by determining its radial distance from the AGN (r_H).

First, we estimate r_H based on the spatial information given in Section 3.1 and the parameters determined in Section 4.1. The ionizing luminosity (L_{ION}) of the illuminating source is related to the radial distance of the emission region from the ionizing source (r) and the ionization parameter (U) by

$$L_{ION} = 4\pi r^2 U n_H c \langle h\nu \rangle_{ion}, \tag{1}$$

where n_H is the hydrogen density, $\langle h\nu \rangle_{ion}$ is the mean ionizing photon energy[8] and c is the speed of light. Then, solving for the radial distance of the low-ionization/density region, we get

$$r_L^2 = \frac{L_{ION}}{4\pi U_L n_H^L c \langle h\nu \rangle_{ion}} \tag{2}$$

and similarly for the high-ionization/density emission region we have

$$r_H^2 = \frac{L_{ION}}{4\pi U_H n_H^H c \langle h\nu \rangle_{ion}}. \tag{3}$$

---

[8] We assume a value of 56 eV for $\langle h\nu \rangle_{ion}$, which is based on an ionizing power law of -1.2, with the photon energy limits of 13.6 eV and 5 keV.

By combining equations (2) and (3), we obtain an equation which allows us to determine the relative radial distances of the high- and low-density regions from the AGN:

$$\left[\frac{r_{\mathrm{H}}}{r_{\mathrm{L}}}\right]^2 = \frac{U_{\mathrm{L}} n_{\mathrm{H}}^{\mathrm{L}}}{U_{\mathrm{H}} n_{\mathrm{H}}^{\mathrm{H}}}. \tag{4}$$

Using the densities and ionization parameters estimated in Section 4.1, we find that the radial distance of the FHIL emission region ranges from 0.0002 to 0.03 of that of the low-ionization region. As mentioned in Section 3.6, the [O II] $\lambda 3727$ emission is resolved in the 2D spectrum of Q1131+16, and the half width at half-maximum measured for the central peak of this emission line is found to be 0.53 ± 0.05 arcsec (corrected for the seeing). This corresponds to $r_{\mathrm{L}} = 1.7 \pm 0.2$ kpc, implying that the radial distance of the FHIL region from the AGN is in the range $0.30 < r_{\mathrm{H}} < 50$ pc – consistent with recent observational estimates of the size of the torus in nearby AGNs, based on IR interferometry and high-resolution molecular line observations (e.g. Haschick, Baan & Peng 1994; Chou 2007; Tristram et al. 2007). However, we emphasize that this argument assumes that the [O II] emission-line region is solely ionized by the AGN, which may not be true if stellar photoionization is significant at a kpc scale. Also, if the contrast between the conditions in the low- and high-ionization regions is larger than assumed here (see discussion in Section 4.1), the radial distance of the FHIL region from the AGN will be correspondingly lower. Overall, it is likely that this analysis, based on estimates of U and n_{H}, overestimates the true radial distance of the FHIL region.

If the ionizing luminosity (L_{ION}) is known, then it is also possible to estimate the radial distance of the FHIL region from the AGN using equation (1) directly. L_{ION} can be estimated from the bolometric luminosity (L_{BOL}), which itself can be determined from the [O III] $\lambda 5007$ emission-line luminosity ($L_{\mathrm{[O\,III]}}$) by manipulating equation (1) from Dicken et al. (2009)[9] to give

$$L_{\mathrm{BOL}} = \frac{100}{C_{\mathrm{NLR}}} L_{\mathrm{[O\,III]}}, \tag{5}$$

where C_{NLR} is the NLR covering factor. Assuming typical NLR covering factors in the range $0.02 < C_{\mathrm{NLR}} < 0.08$ (Netzer & Laor 1993), we estimate a bolometric luminosity in the range $3 \times 10^{38} < L_{\mathrm{BOL}} < 10^{39}$ W [Correction added after online publication 2011 May 24: L_{BOL} range amended].

Alternatively, we can use our knowledge of the likely geometry of the FHIL to estimate an upper limit on the covering factor of the FHIL region and a lower limit on L_{BOL}. Assuming that the FHILs are emitted by the inner wall of the torus on the far side of the AGN (see Section 4.3), we see a maximum of 25 per cent of the total area of the inner wall of the torus (with the rest obscured). A typical torus with an opening half-angle of $45°$ has a *total* covering factor of $C_{\mathrm{torus}} = 0.7$. Therefore, for our assumed geometry, an upper limit on the covering factor of the FHIL region is $C_{\mathrm{FHIL}} = 0.7 \times 0.25 = 0.175$. Substituting this into equation (5), we obtain the following lower limit on the bolometric luminosity: $L_{\mathrm{BOL}} > 10^{38}$ W.

We convert L_{BOL} to L_{ION} using the relationship given in Elvis et al. (1994) ($L_{\mathrm{BOL}} \approx 3.1 L_{\mathrm{ION}}$), which leads to $3 \times 10^{37} < L_{\mathrm{ION}} < 10^{38}$ W. Then, using equation (1) and the model parameters from Section 4.1, we estimate the radial distance of the FHIL region from the AGN to be in the range $0.3 < r_{\mathrm{H}} < 10$ pc. For comparison, based on our estimates of the AGN bolometric luminosity, the sublimation

radius of the dust grains in the torus[10] is $0.26 < r_{\mathrm{sub}} < 0.52$ pc – consistent with the lower end of the range of our estimates of r_{H}. This consistency supports the idea that the FHILs are emitted by the inner torus wall.

4.5 The unusual strength of the FHIL

It is also important to consider why the FHILs are so much stronger in Q1131+16 and other similar objects than in more typical AGNs.

First, we must consider the possibility that, rather than an AGN, the spectrum of Q1131+16 is the result of a supernova, in particular a Type IIn supernova. Type IIn supernova are a subclass of supernovae for which it is believed that the supernova progenitor has undergone mass stripping of its outer layers in the late stages of its life. This process introduces a dense hydrogen gas in the circumstellar medium surrounding the progenitor. The shockwave from the supernova interacts with the material, heating it. This results in a rich spectrum of narrow emission lines, which has some similar characteristics to the spectrum of Q1131+16 (Smith et al. 2009). It is notable that early observations of the [Fe VII] emission lines in one such supernova, SN 2005ip (see Smith et al. 2009), indicate electron densities of 10^8 cm^{-3} and higher (Smith et al. 2009).

One argument against this suggestion is that the [O III] $\lambda 5007$ luminosity of Q1131+16 exceeds that of the hottest known Type IIn supernova by three orders of magnitude (Smith et al. 2009). Also the line emission from a supernova is expected to be variable. In the case of the Type IIn supernova considered by Smith et al. (2009), [O III] $\lambda 5007$ increased eight-fold after 100 d and then faded to half this intensity after 3 yr. The [Fe VII] $\lambda 5720$ emission line decreased four-fold in intensity after 100 d, but after 3 yr, this intensity had increased to half its original intensity. As for the [Fe VII] $\lambda 6086$ emission line, this decreased in intensity by half after 100 d and then varied over 3 yr around half its original intensity. However, in Q1131+16 there is no evidence for emission lines fading in the 3 yr between the WHT and Gemini spectra. This lack of variability rules out any supernova component.

The lack of variability in the emission lines of Q1131+16 also provides strong evidence against the idea that its unusual FHILs are due to an illumination flare caused by the tidal disruption of a star by the SMBH (Komossa, Zhou & Lu 2008). In the well-studied case of SDSS J095209.56+214313.3 (Komossa et al. 2009), FHILs, such as [Fe VII] $\lambda\lambda 3759,5159$, were seen to dramatically vary over a time-scale of 3 yr: the [Fe VII] $\lambda 3759$ line[11] by 36 per cent in intensity over 3 yr, the [Fe VII] $\lambda 5159$ line by 79 per cent and the He II $\lambda 4686$ line by 65 per cent. In contrast, the same lines in Q1131+16 did not vary significantly over a similar 3-yr time-scale. Moreover, the Balmer lines in Q1131+16 lack the variable, multipeaked profiles observed in SDSS J095209.56+214313.3 (Komossa et al. 2008; Komossa et al. 2009).

Rather than an illumination event, an explanation for the unusual strength of the FHILs may by provided by the inner torus wall being viewed at a specific orientation at which the inner wall on the far side of the torus can be seen by the observer, but the quasar itself remains hidden, because the torus is being viewed at a relatively large angle to its axis (see Section 4.3). In this case, the visible area of the torus wall is large enough that the FHILs are strong,

---

[9] Assuming $L_{\mathrm{[O\,III]}} = 5.5 L_{\mathrm{H}\beta}$ rather than $L_{\mathrm{[O\,III]}} = 12 L_{\mathrm{H}\beta}$.

[10] We calculate the sublimation radius using the expression for the AGN sublimation radius given in Elitzur (2008).

[11] Here all ratios are relative to [O III] $\lambda 5007$. In SDSS J095209.56+214313.3, the [O III] flux varies very little between the spectra (see Komossa et al. 2009).
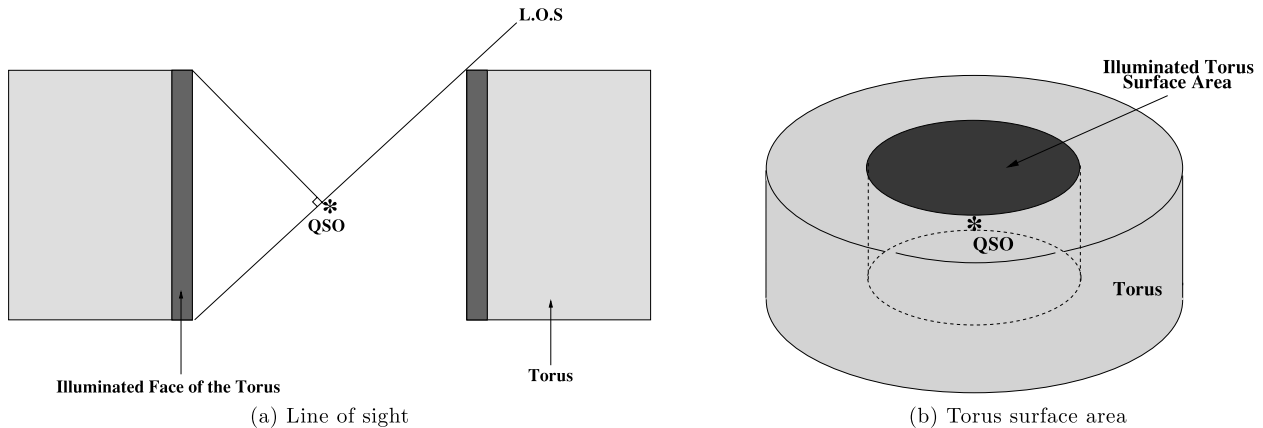
(a) Line of sight   (b) Torus surface area

Figure 22. (a) Schematic displaying an edge-on view of the possible observed orientation of the AGN in Q1131+16. (b) Schematic displaying the visible area of the inner torus wall of Q1131+16 as viewed by the observer. This special geometry will maximize the observed emission-line flux of the inner wall of the torus yet still obscure the central quasar, thus lowering the underlying continuum, and hence resulting in FHILs with large EWs.

but the direct quasar continuum emission does not dilute the torus line emission (see Fig. 22). Therefore, the FHILs are observed with large EWs. Viewed at smaller angles to the axis of the torus, the luminous quasar nuclear emission would become directly visible, substantially reducing the EWs of the FHILs.

In this context, we note that, despite the unusually large EWs of its FHILs, the measured ratios of the FHILs to lower ionization lines (e.g. [Fe VII]/[O III], [Fe VII]/[S II], [Fe VII]/[O I] and [Fe X]/[O I]) for Q1131+16 fall well within the ranges measured for typical broad-line AGNs (Seyfert 1, Seyfert 1.5, narrow-line Seyfert 1) in the sample compiled by Nagao et al. (2000). Therefore, viewed from a direction closer to the torus axis, we would expect Q1131+16 to display a normal quasar/Seyfert 1 spectrum, but the multitude of fainter FHILs would be difficult to detect because of the dilution by the bright quasar continuum and broad-line emission.

However, it is more challenging to explain why the FHILs are significantly stronger relative to the low-ionization lines in Q1131+16 than in typical Type 2 AGNs (Nagao et al. 2000). Given the geometry in Fig. 22, we would expect to observe significant FHIL emission over a range of viewing angles, even if the quasar nucleus itself is obscured; rather than a sharp cut-off, for this simple geometry, the strength of the FHIL would gradually diminish as the orientation of the axis of the torus to the line of sight is increased (i.e. the torus becomes more edge-on). Therefore, although the particular geometry shown in Fig. 22 would maximize the FHIL emission, it is unlikely that a specific geometry alone can explain the rarity of objects like Q1131+16. We now discuss three further factors that might lead to the FHIL appearing relatively strong compared with the general population of Type 2 AGNs.

(i) *A lack of conventional NLR emission.* If the emission from a 'conventional' NLR on a scale of ~0.1–1 kpc were strong, then this would dilute the FHIL emission and the overall spectrum would not appear unusual relative to other Type 2 AGNs. Therefore, the conventional NLR emission must be relatively weak in the case of Q1131+16 and other similar objects. Weak NLR emission can arise if the covering factor of the NLR is relatively small or if the illuminating AGN has only recently been triggered (within the last 100–1000 yr), so that the ionizing radiation has not had time to traverse the scale of the NLR. However, while the lack of a conventional NLR might help to explain the unusual emission-line ratios, it would not explain the unusually high EWs measured

for many of the emission lines in Q1131+16. Indeed, if this was the dominant factor, then we would expect the emission lines in Q1131+16 to have *lower* EWs than most other Type 2 AGNs, which is clearly not the case.

(ii) *A lack of obscuration by large-scale dust structures that are not coplanar with the torus.* Along with a compact torus on a scale of 1–100 pc, many active galaxies show evidence for larger dust lane structures on a scale of 100 pc–5 kpc. If the dust lanes are not exactly coplanar with the torus structures (e.g. thicker or different orientation), then they will make it more difficult to observe the inner face of the torus, thus reducing the strength of the optical FHIL emission and narrowing the range of angles over which the FHIL would appear strong. While the lack of such large-scale dust structures would certainly increase the chance of observing unusually strong FHILs, their presence would in any case reduce the range of viewing angles over which the FHIL would be visible.

(iii) *A recently triggered AGN.* If the AGN has only recently been triggered, then not only might this result in reduced emission from the conventional NLR (see above), but also the inner wall of the torus itself might not yet have reached an equilibrium radius set by dust sublimation. In this case, the clouds close to the AGN are likely to be in the process of evaporation by the strong AGN radiation field (Pier & Voit 1995) and, depending on the density gradient, might have a higher ionization parameter than clouds at the sublimation radius, leading to relatively strong FHIL. The problem with this explanation for Q1131+16 is that the radius of the FHIL emission-line region is similar to the estimated sublimation radius of the torus (see Section 4.4), suggesting an equilibrium situation. However, it is possible that future refinement of the physical conditions of the FHIL in Q1131+16 and the bolometric luminosity of its AGN might lead to a revision of this picture.

Overall, while a specific viewing angle is likely to provide an important part of the explanation for the unusual spectrum of Q1131+16, one or more of the other factors discussed above may also be significant.

4.6 Q1131+16 in relation to other similar objects

As mentioned previously, there are a few similar objects in which the FHILs are unusually strong (III Zw 77, Tololo 0109-383 and ESO 138 G1). The key properties of these objects, as derived from

Table 6. Table comparing key properties determined for the FHIL regions of Q1131+16, III Zw 77 (Osterbrock 1981), Tololo 0109-383 (Fosbury & Sansom 1983; Murayama & Taniguchi 1998) and ESO 138 G1 (Alloin et al. 1992).

Object	Density (cm^{-3})	Velocity width (FWHM, $km\,s^{-1}$)	[O III] (5007/4363)
Q1131+16	$10^8 > n_H > 10^5$	361 ± 29	5.86 ± 0.21 (WHT)
III Zw 77	$n_e > 10^5$	$\sim400^a$	11.48 ± 0.02
Tololo 0109-383	$n_e > 10^6$	~330	21.50 ± 0.46
ESO 138 G1	$n_e > 10^5$	~1000	30 ± 2

^{a}Shows a systematic in line width increase from low- to high-ionization lines.

their FHILs, are presented in Table 6. In particular, we note that the densities derived from the FHILs are consistently high. Also all the objects show a particularly low [O III] (5007/4363) line ratio when compared to 'typical' Seyfert galaxies (although in this respect Q1131+16 is the most extreme). Finally, all the objects show relatively modest FHIL linewidths (FWHMs), with the exception of ESO 138 G1 whose linewidths are larger.

Because there are relatively few objects with such unusual features, it is entirely plausible that the properties of all these objects can be explained in a similar way, for example, with a specific viewing angle of the torus that maximizes the observed emission area of the torus whilst still obscuring the central engine, consistent with the scheme described by Murayama & Taniguchi (1998), Nagao et al. (2001) and Nagao et al. (2000).

5 CONCLUSIONS

Q1131+16 has a remarkable spectrum which displays a multitude of FHILs of relatively high EWs, as well as the more common emission lines expected of an AGN spectrum.

An in-depth study of the spectrum of Q1131+16 has revealed:

(i) emission-line ratios for the FHIL region that are consistent with high densities ($10^{5.5} < n_H < 10^{8.0}\ cm^{-3}$) and ionization parameters ($-1.5 < \log[U] < 0$);

(ii) similar velocity widths (FWHMs) for the low- and high-ionization lines, and a lack of evidence for substantial velocity shifts of the FHILs relative to the galaxy rest frame; and

(iii) a small radial distance from the AGN for the region emitting the FHILs ($0.30 < r_{FHIL} < 50\,pc$).

Based on the high densities and relatively quiescent kinematics implied by our observations, it is likely that the FHILs in Q1131+16 are emitted by the torus wall, with the inner wall on the far side of the torus viewed directly by the observer, but the quasar itself remaining hidden. This geometry is also consistent with the relatively small radial distance found for the FHIL region.

These results demonstrate the potential of the FHILs for probing the circumnuclear obscuring regions in AGNs.

REFERENCES

Alloin D., Bica E., Bonatto C., Prugniel P., 1992, A&A, 226, 117
Antonucci R. R. J., 1993, ARA&A, 31, 473
Antonucci R. R. J., Miller J. S., 1985, ApJ, 297, 621
Appenzeller I., Östreicher R., 1988, AJ, 95, 45
Appenzeller I., Wagner S. J., 1991, A&A, 250, 57
Chou R. C. Y., 2007, ApJ, 670, 116
Cutri R. M., 1995, A&AS, 187, 7509
Dicken D., Tadhunter C., Axon D., Morganti R., Inskip K. J., Holt J., González Delgado R., Groves B., 2009, ApJ, 694, 268
Elizur M., 2008, New Astron. Res., 52, 274
Elvis M. et al., 1994, ApJS, 95, 1
Ferguson J. W., 1997, ApJS, 110, 287
Ferland G. J., 1998, PASP, 110, 761
Fosbury R. A., Sansom A. E., 1983, MNRAS, 204, 1231
Gaskell C. M., Ferland G. J., 1984, PASP, 96, 393
Grevesse N., Anders E., 1989, in Waddington C. J., ed., AIP Conf. Proc. Vol. 183, Cosmic Abundances of Matter. Am. Inst. Phys., New York, p. 1
Grevesse N., Noels A., 1993, in Prantzos N., Vangioni-Flam E., Casse M., eds, Origin & Evolution of the Elements. Cambridge Univ. Press, Cambridge, p. 15
Haschick A. D., Baan W. A., Peng E. W., 1994, ApJ, 437, 35
Hutchings J. P., Maddox N., Cutri R. M., Nelson B. O., 2003, AJ, 126, 63
Kaler J. B., 1976, ApJS, 31, 517
Komossa S., Zhou H., Lu H., 2008, ApJ, 678, 81
Komossa S. et al., 2009, ApJ, 701, 105
Korista K. T., Ferland G. J., 1989, ApJ, 343, 678
Manchado A. et al., 1998, in Fowler A. M., ed., SPIE Proc. Vol. 3354, Infrared Astronomical Instrumentation. SPIE, Bellingham, p. 448
Meinel A. B., Aveni A. F., Stockton M. W., 1975, Catalogue of Emission Lines in Astrophysical Objects. Optical Sciences Center, Univ. Arizona, Tucson
Mullaney J. R., Ward M. J., 2008, MNRAS, 385, 53

Mullaney J. R., Ward M. J., Done C., Ferland G. J., Schurch N., 2009, MNRAS, 394, 16

Murayama T., Taniguchi Y., 1998, ApJ, 497, 9

Nagao T., Taniguchi Y., Murayama T., 2000, AJ, 119, 2605

Nagao T., Murayama T., Taniguchi Y., 2001, ApJ, 549, 155

Nagao T., Murayama T., Shioya Y., Taniguchi Y., 2003, AJ, 125, 1729

Netzer H., Laor A., 1993, ApJ, 404, 51

Nussbaumer H., Osterbrock D. E., 1970, ApJ, 161, 811

Nussbaumer H., Storey P.J, 1982, A&A, 1131, 21

Oke J. B., Sargent W. L. W., 1968, ApJ, 151, 807

Osterbrock D. E., 1978, Phys. Scr., 17, 285

Osterbrock D. E., 1981, ApJ, 246, 696

Osterbrock D. E., Ferland G. J., 2006, Astrophysics of Gaseous Nebulae and Active Galactic Nuclei, 2nd edn. University Science Books, Mill Valley, CA

Paglione T. A. D., Timothy A. D., Jackson J. M., Bolatto A. D., Heyer M. H., 1998, ApJ, 493, 680

Penston M. V., Fosbury R. A. E., 1978, MNRAS, 185, 479

Penston M. V., Fosbury R. A. E., Boksenberg A., Ward M. J., Wilson A. S., 1984, MNRAS, 208, 347

Peterson B. M., 1997, An Introduction to Active Galactic Nuclei. Cambridge Univ. Press, Cambridge

Pier E. A., Voit G. M., 1995, ApJ, 450, 628

Ralchenko Yu., Kramida A. E., Reader J., NIST ASD Team, 2010, NIST Atomic Spectra Database (version 4.0), [Online]. Available: http://physics.nist.gov/asd.National Institute of Standards and Technology, Gaithersburg, MD

Ramos Almeida C., Pérez García A. M., Acosta-Pulido J. A., 2009, ApJ, 694, 1379

Robinson A., Binette L., Fosbury R. A. E., Tadhunter C. N., 1987, MNRAS, 227, 97

Schlegel D. J., Finkbeiner D. P., Davis M., 1998, ApJ, 500, 525

Siegel W., Migdalet J., Kim Y.-K., 1998, At. Data Nucl. Data Tables, 68, 303

Smith N. et al., 2009, ApJ, 695, 1334

Spergel D. N. et al., 2003, ApJS, 148, 175

Tran H. D., Cohen M. H., Ogle P. M., Goodrich R. W., di Serego Alighieri S., 1998, ApJ, 500, 660

Tristram K. R. W., Meisenheimer K., Jaffe W., Cotton W. D., 2007, in Karas V., Matt G., eds, Proc. IAU Symp. Vol. 238, Black Holes from Stars to Galaxies – Across the Range of Masses. Cambridge Univ. Press, Cambridge, p. 93

Weedman D. W., 1971, ApJ, 167, 23

Zakamska N. L. et al., 2003, AJ, 126, 2144

This paper has been typeset from a TEX/LATEX file prepared by the author.